ACS OMEGA

http://pubs.acs.org/journal/acsodf

Article

Pore Structure Characterization of Eocene Low-Permeability Sandstones via Fractal Analysis and Machine Learning: An Example from the Dongying Depression, Bohai Bay Basin, China

Yan Lu and Keyu Liu*

Cite This: *ACS Omega* 2021, 6, 11693−11710

Read Online

ACCESS | Metrics & More | Article Recommendations

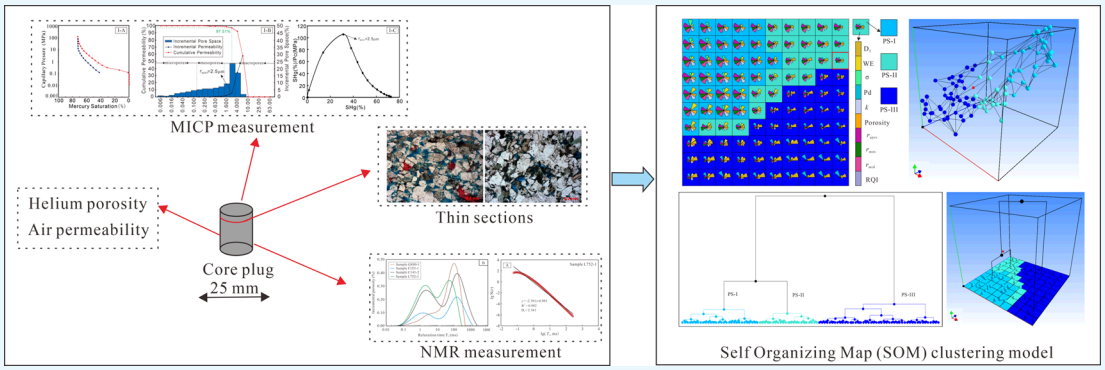

ABSTRACT: Poroperm analysis, mercury injection capillary pressure (MICP), and nuclear magnetic resonance (NMR) measurements were performed to delineate the pore structures and fractal behaviors of the Eocene low-permeability sandstones in the Dongying Depression, Bohai Bay Basin, China. Three types of pore structures (I, II, and III) have been classified by applying the self-organizing map (SOM) clustering model. Comparative analysis of three different fractal models indicates that the MICP tubular model and NMR model are quite effective for pore structure characterization. The results show that the reservoirs generally exhibit high fractal dimensions, indicative of complex pore structures. The presence of small pore throats is primarily responsible for the heterogeneities and complexities in the Eocene low-permeability sandstones. A modified Winland model was established for the permeability estimation using MICP data. Different from high-permeability reservoirs or unconventional (e.g., shale and tight formation) reservoirs, r_{10} is the best parameter for permeability estimation, indicating that the permeability of the Eocene low-permeability sandstones is largely controlled by the large pore systems. Additionally, a porosity model derived from movable fluids using NMR data has been established and provided better prediction effect compared with the classic Coates and Schlumberger Doll Research (SDR) models. Fractal analysis and permeability estimation are shown to be quite effective for investigating microscopic behaviors and in predicting the reservoir quality of low-permeability sandstone reservoirs.

1. INTRODUCTION

The Eocene low-permeability sandstones (permeability: 0.1−50 mD) are the most important reservoir type in the Dongying Depression with great potential for hosting oil and gas.[1−3] The microscopic pore structure features, including the geometric shape, type, size, distribution, and connectivity, determine the reservoir petrophysical properties and thus control the fluid flow in reservoir sandstones. Investigation of microscopic pore structures is thus vital for refined reservoir characterization and improving the efficiency of oil/gas development.[4,5]

The traditional methods such as the Euclidean geometry and experimental techniques are no longer effective in characterizing and evaluating complex and heterogeneous pore structures.[6] Numerous studies have demonstrated that pore structures in porous rocks are self-similar and do not change with investigation scales.[7,8,36] By applying the fractal theory, complex pore systems can be quantitatively investigated,[9−11] and the fractal dimensions obtained can also be applied for reservoir quality evaluation and estimation of petrophysical properties.[12] Fractal analysis has been shown to be especially suitable for characterizing low-permeability terrestrial sandstones that have undergone complex diagenetic modifications.[48]

Received: February 24, 2021
Accepted: April 13, 2021
Published: April 23, 2021

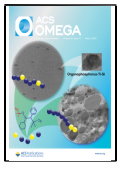

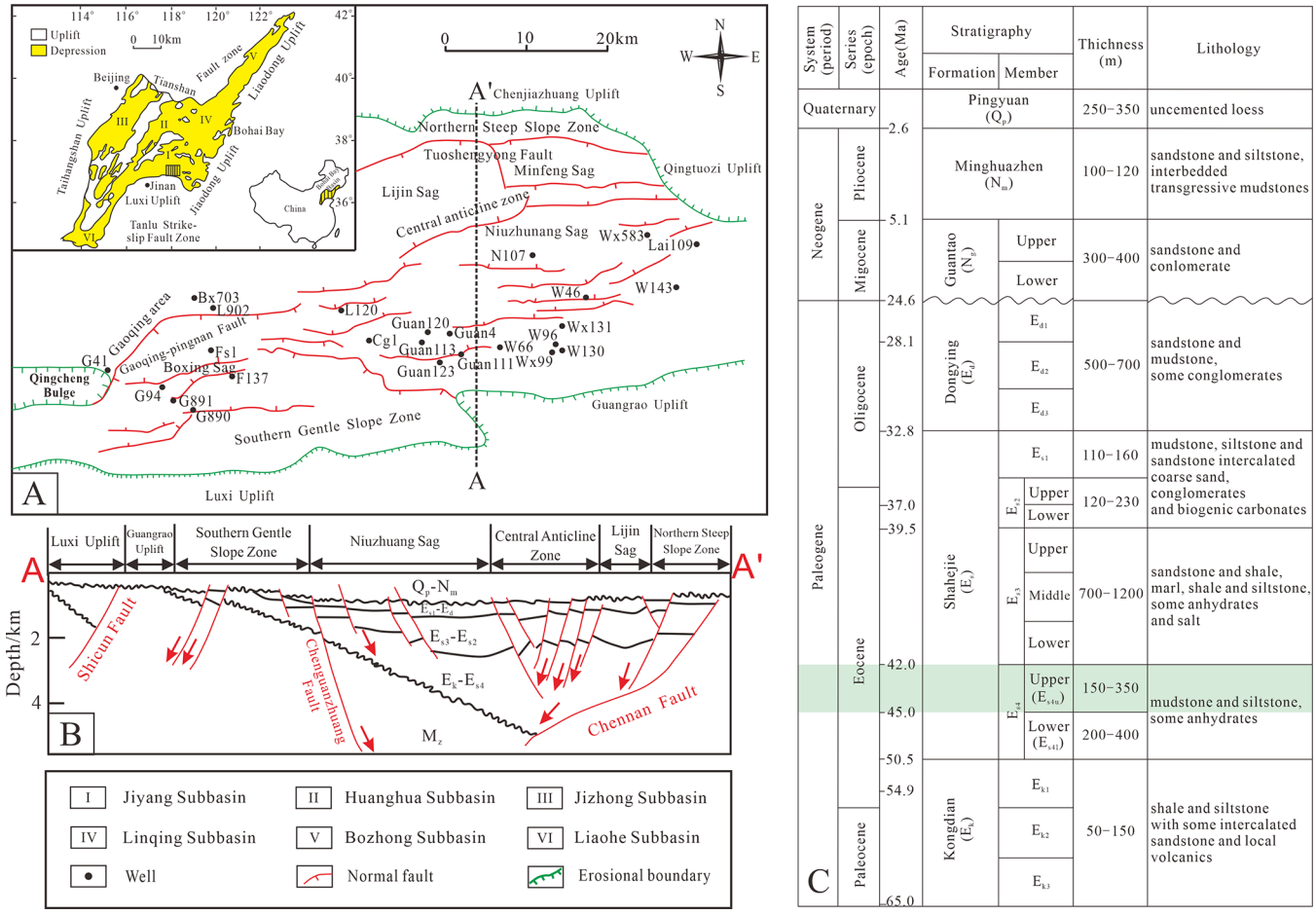

Figure 1. (A) Location of the Dongying Depression in the Bohai Bay Basin, China; (B) cross section showing major structural units and stratigraphic configurations; and (C) generalized stratigraphic column of the Paleogene formations in the study area. Adapted in part with permission from ref 39. Copyright 2020 Elsevier.

Methods applied to analyze the fractal behavior of pore structures include thin sections and scanning electron microscopy (SEM),[13] MICP,[14] NMR,[15−17] X-ray computer tomography,[18,19] and gas adsorption measurements.[20,21] Fractal models established using data sets obtained from the above mentioned methods have advantages and limitations due to their different theoretical principles.[22,23] Hence, fractal characterization of pore structures by an integrated method is commonly used lately.[24,25] Several studies also compared fractal dimensions determined using different techniques.[26,27] Evaluation of different fractal models is helpful to reveal the limitations and advantages of various models, which is crucial for promoting the application and development of the fractal theory in pore structure evaluation. In addition, previous pore structure identification methods such as the morphological analysis or regression analysis of MICP/NMR data are no longer effective and adequate.[27,28] In this paper, a multivariate cluster analysis based on multiple measured variables and machine learning was performed to identify the microscopic pore structure types.

Permeability is an essential parameter in reservoir characterization and controls the ability of fluid flow. It is closely related to pores and pore structures. Numerous studies have been involved in extracting essential attribute parameters from MICP and NMR data for permeability estimation.[29−32] Various empirical permeability models have been established, including Kozeny−Carman (KC) equation,[33,34] PaRiS equation,[35] Winland model,[29,36,37] SDR and Coates model,[30,31] and so forth. Previous studies indicated that the optimal pore throat radius and pore type for permeability estimation are variable in different types of reservoirs.[38] Consequently, investigation of pore structures and its heterogeneity on permeability would be conducive to accurately estimate permeability.

In this study, the fractal behavior of low-permeability sandstones from the Dongying Depression was investigated using MICP and NMR data. The SOM model was employed for pore structure classification using 70 groups of core data. The petrophysical features of various pore structures were analyzed by MICP and NMR data. The relationships between pore structure, petrophysical properties, and fluid mobility were also investigated. A comparative analysis of fractal dimensions using three different fractal models was carried out. Additionally, the effects of pore structures on permeability were discussed and empirical equations for permeability estimation have been established based on capillary pressure curves and NMR T_2 spectral parameters. This study attempts to provide an essential workflow for characterizing fractal behaviors of pore structures and an effective method for estimating permeability and evaluating reservoirs with low-permeability and strong heterogeneities.

https://doi.org/10.1021/acsomega.1c01015
ACS Omega 2021, 6, 11693−11710

2. GEOLOGICAL BACKGROUND

The Dongying Depression is a dustpan-shaped depression developed in the southwestern Bohai Bay Basin, China.[39] It is composed of five structural units, including the northern steep slope zone, northern sag zone (Lijin and Minfeng sags), central anticline zone, southern sag zone (Niuzhuang and Boxing sags), and southern gentle slope zone (Figure 1A,B).[40] The Dongying Depression comprises a thick Paleogene sediment sequence, including the Kongdian, Shahejie, and Dongying formations. The Eocene Shahejie (E_s) Formation is composed of four sedimentary units from bottom to top: E_{s4}, E_{s3}, E_{s2}, and E_{s1} (Figure 1C). The upper E_{s4} (E_{s4u}) unit is considered as the target interval of the study area, and the burial depth of E_{s4u} varies from 2160 to 3563 m. The E_{s4u} unit was deposited in shore-shallow lacustrine environments and consists mainly of fine-grained sandstone interbedded with thin mudstone (Figure 1C).[1]

3. SAMPLING AND METHODOLOGY

3.1. Samples and Analytical Techniques. A total of 70 core plug samples (50 mm long and 25.4 mm in diameter) from different depths were collected from 38 wells located in the Dongying Depression. All samples were subjected to petrophysical property analysis and MICP analysis, among which 32 samples were selected for optical petrographic analysis and 21 samples were selected for NMR measurements (Table 1).

Table 1. Information of Samples and Various Measurements

measurements	number of wells	number of sandstone samples
helium porosity	38	70
air permeability	38	70
thin sections	21	32
MICP	38	70
NMR	12	21

Helium porosity and air permeability were performed to investigate the petrophysical properties of the sandstone reservoirs. Pore structure features of 70 samples were detected by MICP analysis, with the maximum mercury inlet pressure up to 116 MPa. NMR measurements were conducted to extract the T_2 spectra of 21 samples. First, the NMR T_2 spectra at the 100% water-saturated state were measured, with an echo interval of 0.21 ms. The experimental temperature was kept in 25 °C. Then, the samples were centrifuged with a rotating speed of at least 6000 rpm for removing the free water in the plugs and measured again to obtain NMR T_2 spectra under a centrifuged state. It should be mentioned that Sample Cn371-1 is not well-consolidated; thus, only the T_2 spectra at the 100% water-saturated state were measured.

3.2. Fractal Theory. *3.2.1. Fractal Models for MICP Data.* According to fractal theory, self-similar fractal behavior does not change with the scale of magnification.[10,22,41] Since its introduction by Mandelbrot in 1977, it has been widely used in pore structure evaluation and characterization.[42,43] The self-similarity behavior of pore structures can be illustrated by eq 1.[7,44]

$$N(r) \propto r^{-D_f} \tag{1}$$

where r is the pore throat radius; $N(r)$ is the number of pores with a radius larger than r; and D_f is the fractal dimension. The fractal dimensions calculated using both the tubular model (model I) and spherical model (model II) are discussed.

3.2.1.1. Fractal Model I. The $N(r)$ can be expressed in eq 2, when using a tubular model.

$$N(r) = \sum_{j}^{n} \frac{V_i}{\pi r_i^2 l} \propto r_i^{-D_f} \tag{2}$$

where $j = i + 1$, V_i is the cumulative mercury intrusion volume at a certain pore radius r_i, and l is the length of a capillary tube. It should be mentioned that $N(r)$ refers to the equivalent number of pores when the pore space is filled by bundles of capillary tubes with radius r_i.[45,46] D_f can be obtained by the slope of the curve of lg $N(r)$ − lg r_i.

By combining with the Young−Laplace equation (eq 3), the fractal model I can also be expressed in another form (eq 4).

$$P_c = \frac{2\sigma \cos\theta}{r} \tag{3}$$

$$S_{Hg} \propto P_c^{-(2-D_f)} \tag{4}$$

where P_c is the capillary pressure (MPa); σ is the surface tension; θ is the contact angle (°); and S_{Hg} is the accumulative mercury saturation, which can be converted with V_{Hg}.[46]

3.2.1.2. Fractal Model II. According to the fractal theory, the saturation of the wetting phase can be expressed as

$$S_w = \frac{V(<r)}{V} = \frac{r^{3-D_f} - r_{min}^{3-D_f}}{r_{max}^{3-D_f} - r_{min}^{3-D_f}} \tag{5}$$

$$S_w = 1 - S_{Hg} \tag{6}$$

where $V(<r)$ is the pore volume with a radius less than r; V is the total pore volume; and r_{max} and r_{min} are the maximum and minimum pore radius, respectively.

For $r_{min} \ll r$, we get

$$S_w = \frac{r^{3-D_f}}{r_{max}^{3-D_f}} \tag{7}$$

By combining eqs 3, 6, and 7 and taking logarithms on both sides of eq 7, it becomes

$$\lg(1 - S_{Hg}) = (D_f - 3)\lg P_c + (3 - D_f)\lg P_{cmin} \tag{8}$$

$$D_f = S + 3 \tag{9}$$

3.2.2. Fractal Dimensions Based on NMR Experiments. Lai et al. (2018) proposed a fractal model using NMR data, and it can reflect the whole pore size distribution.[47] The pores detected by NMR measurement were assumed to be spherical and then the $N(r)$ can be described by eq 10.

$$N(r) = \sum_{j}^{n} \frac{V_{pi}}{\frac{4}{3}\pi r_j^3} = \sum_{j}^{n} \frac{V_{pj}}{36\pi(\rho T_{2j})^3} \tag{10}$$

where V_{pi} is the cumulative pore volume at a given pore radius r_i, ρ is the surface relaxivity, and T_2 is the transverse relaxation time.

By combining eqs 1 and 11

$$N(r) = \sum_{j}^{n} \frac{V_{pj}}{36\pi(\rho T_{2j})^3} \propto (3\rho T_{2i})^{-D_f} \tag{11}$$

Using logarithms for eq 11

https://doi.org/10.1021/acsomega.1c01015
ACS Omega 2021, 6, 11693−11710

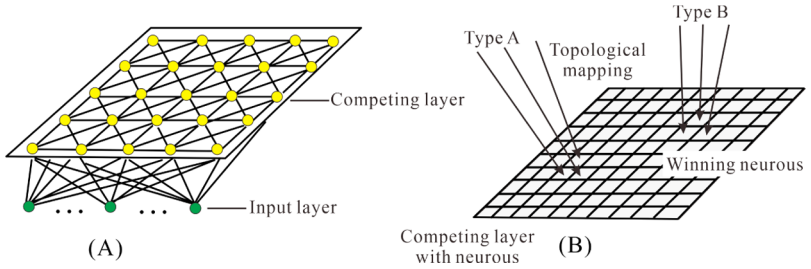

Figure 2. Typical network structure of SOM (A) and competing layer with neurons (B). Adapted in part with permission from ref 39. Copyright 2020 Elsevier; adapted in part with permission from ref 51. Copyright 2015 Wiley-Blackwell.

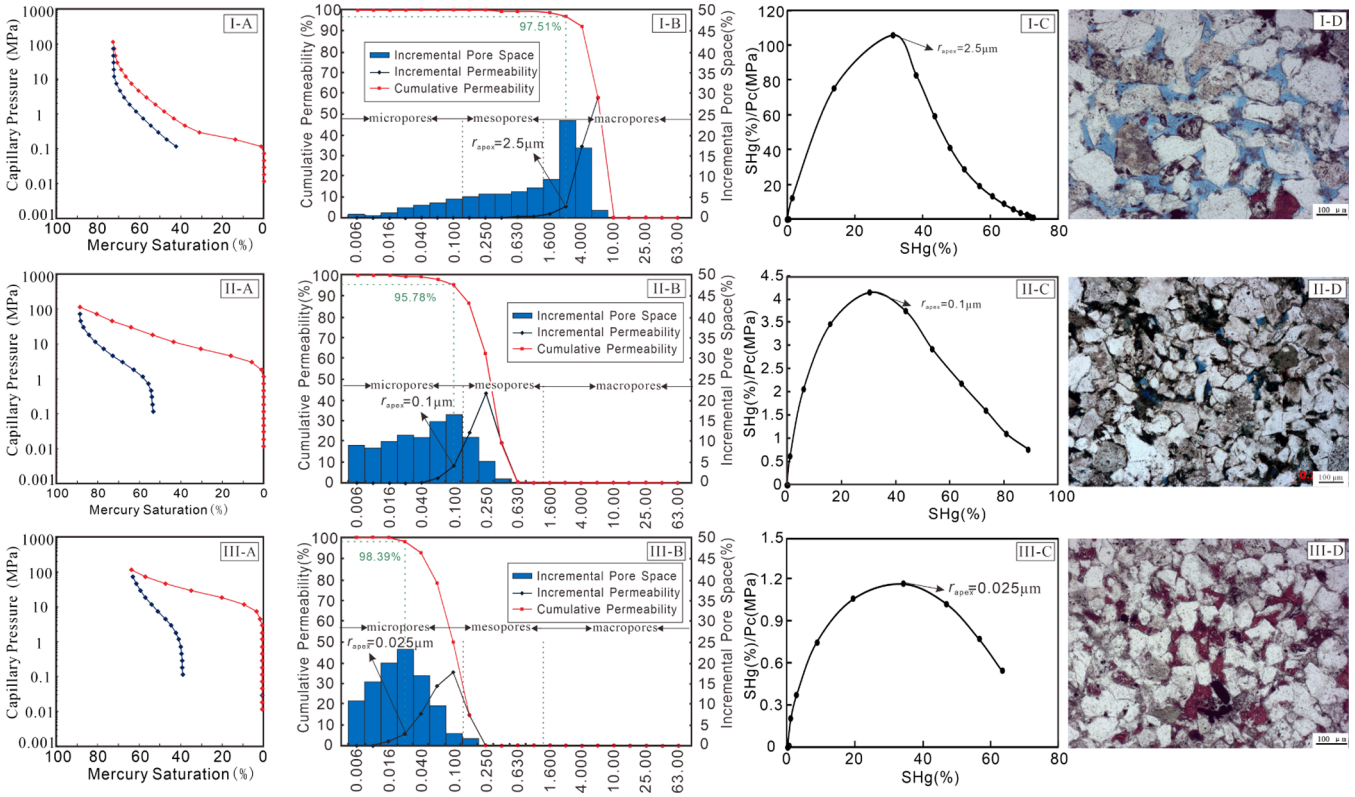

Figure 3. Typical capillary pressure curves (A), pore throat size distribution (B), Pittman's plot (C), and photomicrographs (D) for E_{s4} sandstones derived from MICP measurements and petrographic analysis.

$$\log\left(\sum_{j}^{n}\frac{V_{pj}}{(T_{2j})^3}\right)+\log\left(\frac{1}{36\pi\rho^3}\right) = -D_f\log(3\rho) - D_f\log(T_{2i}) \quad (12)$$

where $\log\left(\frac{1}{36\pi\rho^3}\right)$ and $\log(3\rho)$ are constants. The fractal dimension (D_f) can be calculated from the logarithmic relationships between $\sum_{j}^{n}\frac{V_{pj}}{(T_{2j})^3}$ and T_{2i}.

3.3. SOM Neural Network Algorithm. The SOM neural network algorithm is a clustering analysis method based on unsupervised machine learning.[48,49] The network structure is composed of an input layer and a competing layer (Figure 2). The neuron in the competing layer can automatically compete for the opportunity to respond to the input pattern and adjust the weights W_{ij} by competitive learning.[50] The neuron with the strongest response is known as the winning neuron and is also known as the best matching unit (BMU). After repeated training and weight adjustment, the derived topological mapping can be used for assigning the best fitting category for each input pattern.

The process of weight adjustment is shown as follows

$$D_j = \|x_i - w_{ij}\|, \qquad j = 1,2,\ldots 100 \quad (13)$$

$$P(g) = \max P(j) = \max\frac{(D_j)-\mu}{\sum_{j=1}^{100}(D_j)-\mu} \quad (14)$$

$$W_{ij} = W_{ij} + \eta_1(x_i - W_{ij}) \quad (15)$$

where i and j are neurons in the input layer and the competing layer, respectively; D_j is the Euclidean distance; x_i are the input variables; g is the winning neuron; $P(j)$ is the winning probability; μ is a constant; and W_{ij} is the weight between the neuron i and neuron j.

The advantage of the SOM classifier is that the clustering results are not affected by incorrect user-defined information,[51,52] and there are no restrictions on the number of

https://doi.org/10.1021/acsomega.1c01015
ACS Omega 2021, 6, 11693−11710

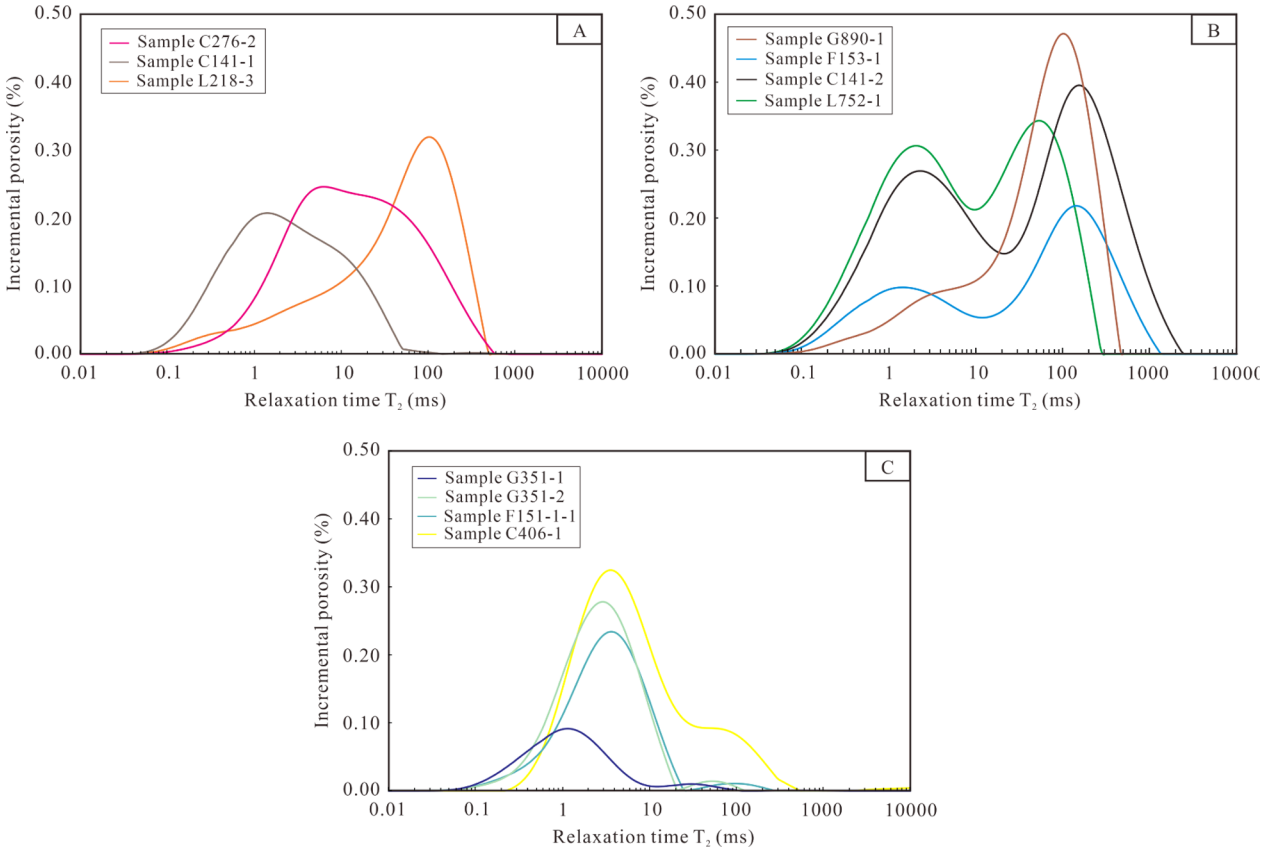

Figure 4. Typical NMR T_2 spectra with unimodal (A) and bimodal behavior [samples with higher right (B) and left peak (C)].

parameters participating in the training process.[53,54] Therefore, the unsupervised neurocomputing algorithm presents an excellent application in solving pattern recognition problems. It provides a way for automatic classification of pore structures.

4. RESULTS

4.1. Pore Structure Characterization. *4.1.1. Pore Structure Characteristics from MICP Analysis.* Highly variable MICP capillary parameters and pore throat size distributions were derived from 70 core samples in the E_{s4} sandstones. The pore structure features were investigated by three typical sandstone groups (Figure 3). The samples with good physical properties (Group I) exhibit a high mercury withdrawal efficiency and a relatively low displacement pressure, which indicates a good pore throat connectivity. The samples also display a wide pore throat size distribution with a pore throat radius mainly in the range of 0.0063−10.0 μm (Figure 3B). The pore systems of Group I are dominated by dissolution pores and residual intergranular pores (Figure 3D). In contrast, the samples with poor physical properties (Group II and Group III) are characterized by high displacement pressures and relatively low mercury withdrawal efficiencies, suggesting that the samples are dominated by small pore throats. The pore throat sizes in samples of Group II and Group III exhibit a narrow distribution, with the pore throat radius being mostly less than 1.0 μm (Figure 3B). The development of small pore throats is commonly associated with incomplete dissolution of clay minerals and clastic particles (Figure 3D).

By plotting S_{Hg} and S_{Hg}/P_c, a sharp apex can be identified,[36] and the pore throat radius corresponding to the apex was defined as r_{apex} by Lai and Wang (2015)[14] (Figure 3C). The pore systems can be separated into large and connected pore systems and small pore systems based on the value of r_{apex}.[14,55] Pore throats with a radius larger than r_{apex} contribute significantly to permeability, whereas the contribution of the small pore throat system ($r < r_{apex}$) to permeability is small (Figure 3B). Therefore, r_{apex} can be used as an important index to evaluate reservoir quality and pore throat connectivity.

4.1.2. Pore Size Distribution Obtained by NMR T_2 Spectra. Previous studies show that the NMR T_2 transverse relaxation time of the hydrogen nucleus is closely related to pore size.[43,56] Samples with short transverse relaxation times indicate the existence of small pores, whereas long transverse relaxation times are often associated with macropores or fractures. The signal amplitude of T_2 transverse relaxation time is indicative of the pore volume fraction with different pore sizes. The NMR T_2 spectra can provide more comprehensive pore structure information compared with the MICP measurements, and the differences among various samples revealed by NMR are more distinct.[57,58]

Figure 4 shows typical NMR T_2 spectral distributions of E_{s4} sandstones, among which three types of NMR T_2 spectral distributions are revealed. Type I T_2 spectra exhibit a continuous unimodal behavior, with T_2 times in the range of 0.01−1000 ms (Figure 4A). Type II T_2 spectra (bimodal behavior with a higher right peak) display a coexistence of large and small pores, and the large pores account for a great proportion (Figure 4B). The left peak varies from 0.1 to 10 ms, while the right peak is in the range of 10−1000 ms (Figure 4B). Type III T_2 spectra (bimodal behavior with a higher left peak) show the lack of the long T_2 components compared with

https://doi.org/10.1021/acsomega.1c01015
ACS Omega 2021, 6, 11693−11710

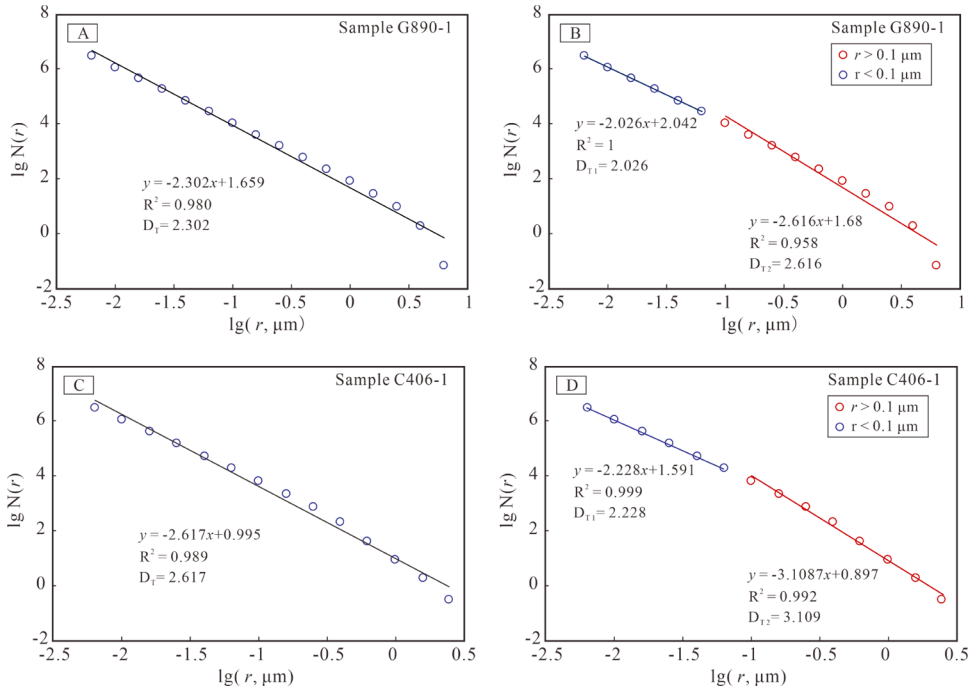

Figure 5. Calculated fractal dimensions using the MICP tubular model. (A,C) Total fractal dimensions (D_T); (B,D) fractal dimensions of small pore systems (D_{T1}) and large pore systems (D_{T2}), respectively.

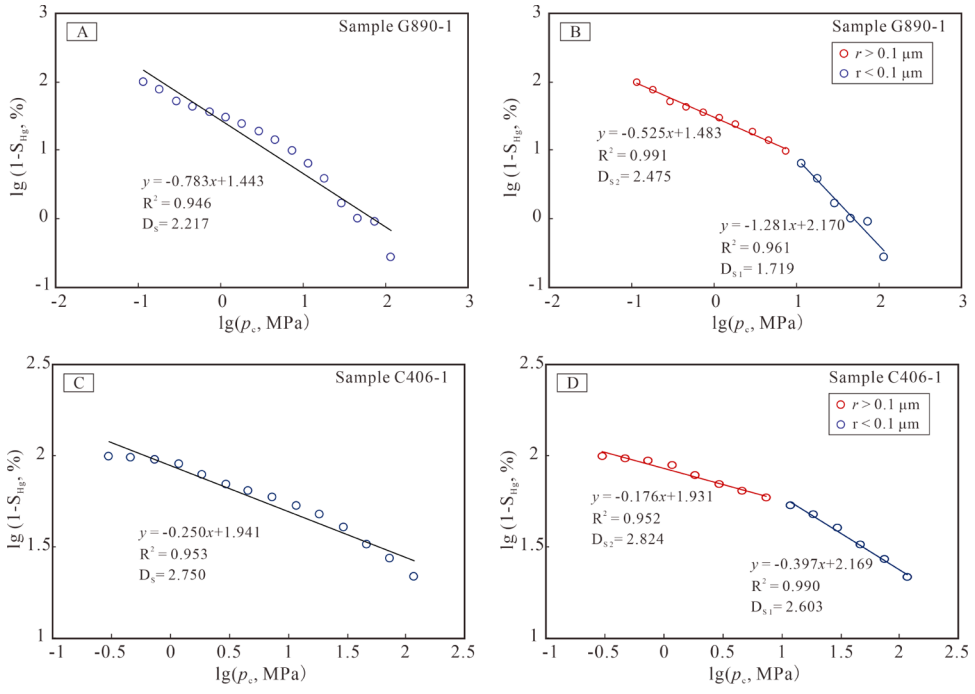

Figure 6. Fractal dimensions obtained using a spherical model. (A,C) Characteristics of total fractal dimensions (D_S); (B,D) fractal dimensions of small pore systems (D_{S1}) and large pore systems (D_{S2}), respectively.

the second type. The T_2 time is mainly concentrated in 0.1−100 ms (Figure 4C).

4.2. Fractal Analysis. *4.2.1. Fractal Dimensions Obtained from MICP Data.* The lg($N(r)$) and lg(r) plots based on the MICP data were constructed for all 70 typical sandstone samples (Figure 5), and the plots show good fits (R^2 > 0.90) (Figure 5). The results indicate that the pore structure derived from the MICP data is characteristic of fractal dimensions and can be characterized using the MICP tubular model. In order to determine the fractal dimensions of small pore systems and large pore systems, the lg($N(r)$) and lg(r) plots were separated into two linear segments using the same segment threshold values (r = 0.1 μm), and the double-fractal characteristics can be approximated by piecewise regression (Figure 5B,D). The fractal dimensions of the left segments (D_{T1}) correspond to the fractal behavior of the small pore systems (r < 0.1 μm), ranging from 2.01 to 2.98 (averaging 2.23). For the right segments, the calculated fractal dimensions (D_{T2}) are characteristic of the

https://doi.org/10.1021/acsomega.1c01015
ACS Omega 2021, 6, 11693−11710

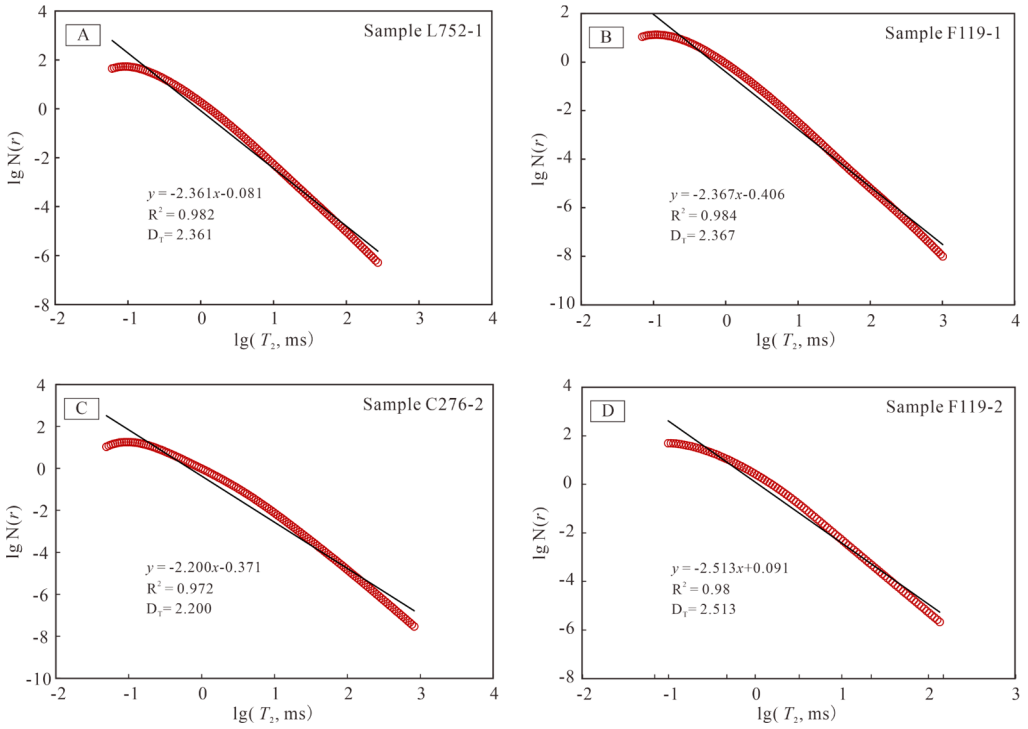

Figure 7. NMR fractal dimensions calculated from the cross-plots of lg $N(r)$ and lg T_2, showing the fractal behavior of the entire pores. (A) Sample L752-1; (B) sample F119-1; (C) sample C276-2; and (D) sample F119-2.

Table 2. NMR T_2 Spectral Parameters and Fractal Dimensions Derived from NMR Data

					$T_2 > T_{2cutoff}$			
sample no	BVI (%)	FFI (%)	S_{mov} (%)	$T_{2cutoff}$ (ms)	D_{mov}	R^2	D_{NMR}	R^2_{NMR}
C276-1	7.30	3.35	31.47	34.36	2.88	0.99	2.40	0.98
C276-2	12.28	4.14	25.21	43.45	2.89	0.99	2.20	0.97
G351-1	2.97	0.73	19.76	2.83	2.96	1.00	2.30	0.96
G351-2	9.31	0.98	9.52	8.96	2.97	1.00	2.32	0.98
G890-1	11.45	7.41	39.29	84.02	2.71	0.99	2.15	0.98
G890-2	2.93	0.44	13.06	5.09	2.97	1.00	2.54	0.98
F151-1-1	8.12	0.57	6.56	12.82	2.93	0.99	2.31	0.98
F153-1	7.94	5.09	39.06	91.99	2.82	0.99	2.40	0.98
C141-1	8.17	3.76	31.52	4.72	2.90	0.99	2.22	0.96
C141-2	6.07	5.48	47.45	41.49	2.84	0.99	2.41	0.97
C406-1	9.44	5.42	36.47	7.97	2.90	0.99	2.14	0.93
F143-1	6.90	3.74	35.15	46.93	2.76	0.99	2.38	0.99
L218-3	9.07	5.61	38.22	76.98	2.73	0.99	2.40	0.99
L218-1	9.59	7.52	43.99	85.61	2.67	0.99	2.16	0.99
L218-2	9.27	6.60	41.59	64.88	2.73	0.99	2.30	0.99
F119-1	7.36	2.76	27.27	150.41	2.84	0.99	2.37	0.98
F119-2	5.11	0.13	2.48	3.95	2.99	1.00	2.51	0.98
G351-1	8.53	1.67	16.37	63.97	2.88	0.99	2.36	0.98
L752-2	6.70	3.09	31.56	5.53	2.92	0.99	2.60	0.99
L752-3	7.33	0.26	3.43	9.88	2.99	1.00	2.31	0.96

large pore systems (r > 0.1 μm). D_{T2} may be greater than 3.0 and shows a broad distribution between 2.32 and 6.54 (averaging 3.53). The presence of microfractures, the use of an oversimplified tubular model, and the skin effect may result in the phenomenon that some samples at the right segments (D_{T2} are greater than 3.0) may not possess fractal characteristics.[59,60]

The log−log plots of 1 − S_{Hg} and p_c based on the spherical model are shown in Figure 6, and the double-fractal characteristics are investigated using the inflection points corresponding to r = 0.1 μm. The detailed fractal dimensions of small pore systems (D_{S1}), large pore systems (D_{S2}), and full range of pore systems (D_S) calculated using a spherical model are shown in Figure 6. The results indicate that the fractal dimensions D_{S1} of some samples appeared to be less than 2.0, which does not conform to the Euclidean dimension and has no significance for pore structure evaluation. For the large pore throats, D_{S2} is in the range of 2.16−2.82 (averaging 2.53), showing strong fractal characteristics.

https://doi.org/10.1021/acsomega.1c01015
ACS Omega 2021, 6, 11693−11710

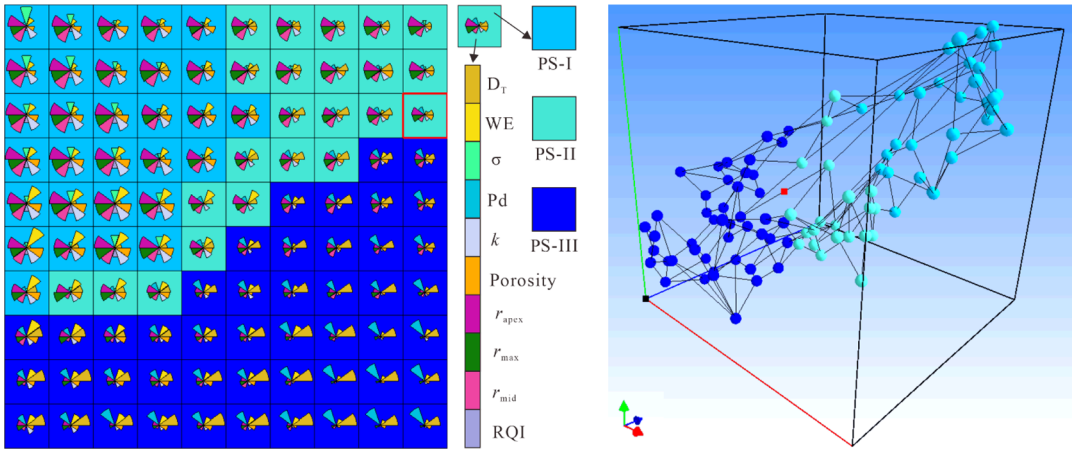

Figure 8. Topological mapping (left) and the related 3D Sammon mapping (right).

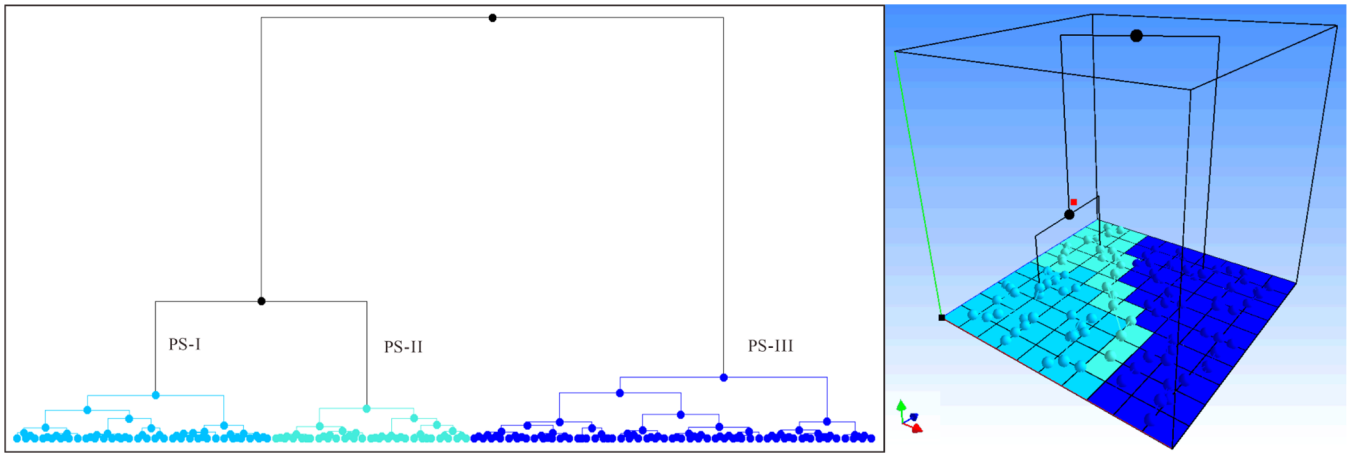

Figure 9. Cluster dendrogram based on the SOM neural network algorithm [2D dimension (left) and 3D dimension (right)], showing the process of pore structure classification.

4.2.2. Fractal Dimensions Derived from NMR Analysis. The log−log plots of V and T_2 are widely used in characterizing the fractal behavior of pore systems.[20,45] However, almost all the researchers indicate that the slope of the linear fitting line in the log−log plot of V and T_2 is not a constant for sandstone samples.[12,23] The slope is steeper when approaching the shorter T_2 times and becomes gentler at longer T_2 times (Figure 7A−D). Previously, it has been a common practice to use the inflection point to segment the curves of lg V and lg T_2 and to define multifractal models.[20,45] However, the criteria for selecting inflection points are not consistent among various published studies, including the $T_{2cutoff}$,[16] T_{2a} (the lowest connection point between the first and the second peak of NMR T_2 spectra) and T_{2b} (nine times of T_{2a}), and T_2 values calibrated by mercury intrusion porosity (MIP).[61]

In this study, the fractal model introduced by Lai et al. (2018)[47] was adopted to describe the fractal behavior of the entire pores. Figure 7 shows a linear relationship between the lg $N(r)$ and lg T_{2i}, and the total fractal dimensions can be derived by the slope of the best fitting line. In addition, the fractal behavior of the pores with a movable fluid can also be determined by the inflection points of $T_{2cutoff}$. The fractal dimensions of the entire pores (D_{NMR}) and pores with a movable fluid (D_{mov}) are summarized in Table 2, and good determination coefficients are identified (Figure 7A−D; Table 2). D_{NMR} and D_{max} are in the range of 2.14−2.60 and 2.67−2.99, respectively (Table 2), indicating that the entire pores and large pores hosting a movable fluid are typical of fractal behavior.

4.3. Pore Structure Identification Based on SOM and Fractal Dimensions. *4.3.1. Preparation of Data.* Various pore structures and petrophysical parameters were selected to characterize the microscopic pore structures. The parameters include porosity (Φ), permeability (k), reservoir quality index (RQI), maximum pore throat radius (r_{max}), median pore throat radius (r_{50}), r_{apex}, displacement pressure (P_d), mercury withdrawal efficiency (WE), sorting coefficient (σ), T_2 geometric mean value (T_{2gm}), median T_2 relaxation time (T_{2mid}), T_2 time corresponding to the highest peak of T_2 spectra (T_{2peak}), free fluid index (FFI), and irreducible water saturation (S_{wi}). In addition, fractal dimensions were also selected to identify the pore structures. Due to insufficient NMR data, only the petrophysical parameters and parameters derived from MICP measurements were used as the input of the SOM model, and the NMR T_2 spectral parameters were used as auxiliary validation. In order to eliminate the dimensional differences, the selected parameters were standardized prior to feeding into the SOM classifier.

4.3.2. Pore Structure Classification. An unsupervised learning strategy was used in pore structure classification, and a 10 × 10 symmetric network was defined. The initial

https://doi.org/10.1021/acsomega.1c01015
ACS Omega 2021, 6, 11693−11710

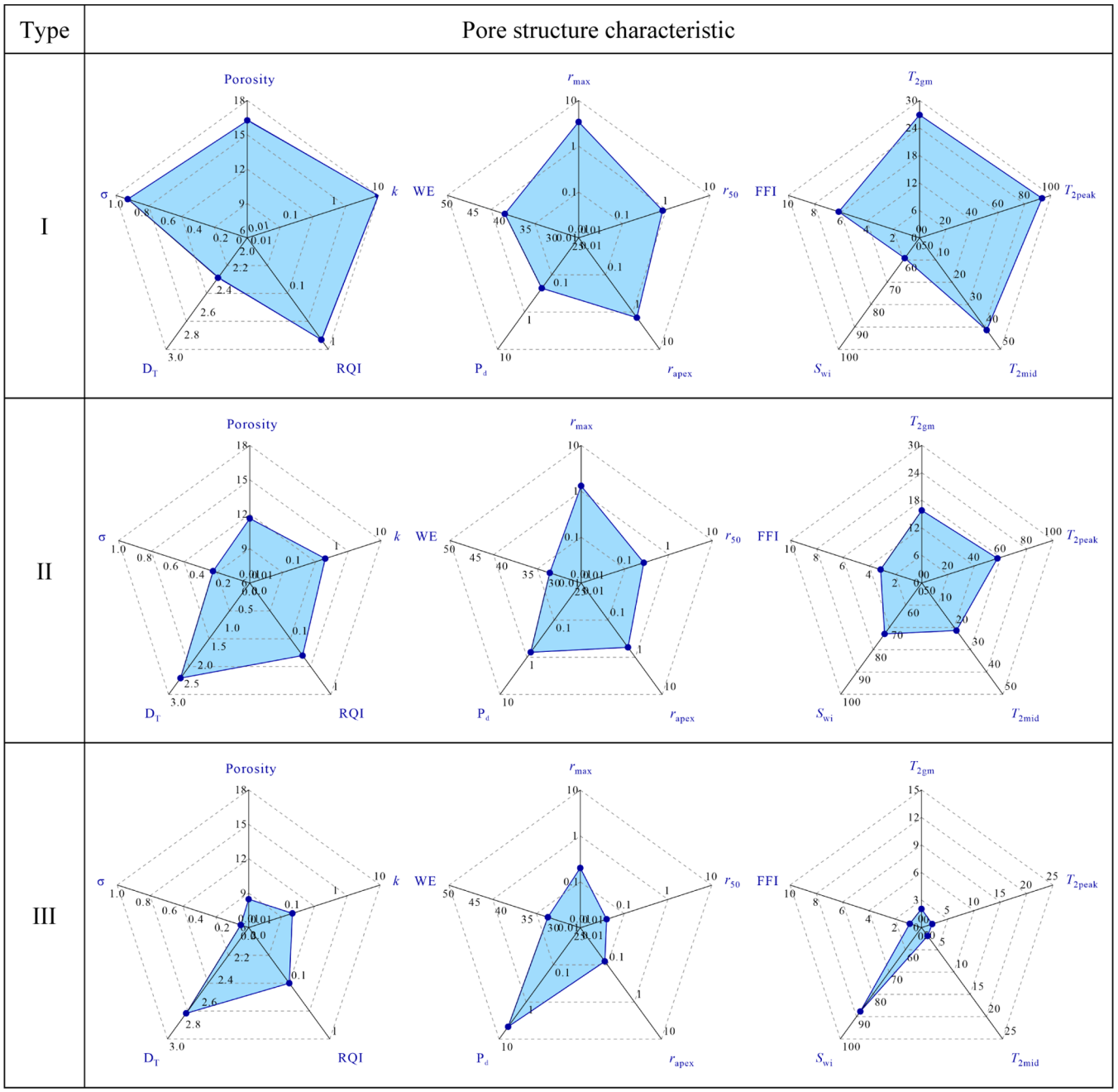

Figure 10. Rider chart showing the characteristics of three types of pore structures.

learning rate was set to 0.5 and the learning process can repeat until the learning rate reduced to 0.0001. The maximum number of iterations was set to 120,000. By assuming three reservoir types, the 70 groups of sandstone samples were clustered into three categories (I, II, and III) by the competitive learning process (Figures 8 and 9). Figure 8 shows the topological self-organized map, showing the clustering result of all sandstone samples. Each neuron represents a specific response of pore structure, and one hundred pore structure features were automatically clustered in the topological map. The rose diagram in each neuron displays a combination of the pore structure and petrophysical parameters (Figure 8). The data points located in the same grid reveal similar pore structure characteristics, whereas the differences among various types of pore structures are significant (Figure 9).

4.3.3. Petrophysical Features of Various Pore Structures. The clustering results show that the Type I pore structure exhibits a good pore throat connectivity and the strongest microheterogeneity (Figure 10 and Table 3). The sandstones dominated by the Type I pore structure are abundant in residual intergranular pores and dissolution pores (Figure 11A,B). Long T_2 components are well-developed in the Type I pore structure, and the r_{50} and r_{apex} are mainly in the range of 0.05−2.36 μm and 0.40−2.50 μm, respectively (Table 3). The Type II pore structure shows a relatively good pore throat connectivity and a strong microheterogeneity. The displacement pressure is relatively high in comparison with those in the type I pore structure (Figure 10 and Table 3). The pore

https://doi.org/10.1021/acsomega.1c01015
ACS Omega 2021, 6, 11693−11710

Table 3. Capillary Parameters and Petrophysical Properties for Three Types of Pore Structures

		PS-I		PS-II		PS-III	
pore structure type		range	average	range	average	range	average
porosity (%)		10.85−24.06	16.26	9.33−14.74	11.63	2.72−13.80	8.47
k (mD)		0.76−54.30	9.81	0.14−1.26	0.53	0.01−0.38	0.10
RQI (μm)		0.24−1.77	0.67	0.11−0.30	0.20	0.04−0.22	0.10
r_{max} (μm)		1.0−8.23	3.39	0.25−3.56	1.31	0.03−0.63	0.20
r_{50} (μm)		0.05−2.36	0.83	0.02−0.67	0.27	0.01−0.15	0.04
r_{apex} (μm)		0.40−2.50	1.42	0.1−1.17	0.54	0.01−0.25	0.08
σ MSE		0.25−1.73	0.91	0.06−0.65	0.28	0.01−0.23	0.06
P_d (MPa)		0.1−0.6	0.23	0.21−10.23	0.73	0.7−20	4.63
WE (%)		22.54−58.91	39.05	18.84−50.25	30.96	14.83−46.79	31.17
T_{2gm} (ms)		6.56−48.74	26.85	7.57−28.62	15.79	1.00−2.99	2.03
T_{2peak} (ms)		3.65−155.52	93.29	6.37−155.22	57.67	1.12−3.65	2.05
T_{2mid} (ms)		4.83−71.80	41.37	7.49−48.32	21.38	0.99−3.07	1.89
S_{wi} (%)		52.55−63.53	59.13	64.85−83.63	72.91	68.44−97.52	87.66
FFI (%)		5.09−7.52	6.16	1.67−4.14	3.13	0.13−3.09	0.89
D_T		2.15−2.62	2.36	2.35−2.83	2.56	2.47−2.98	2.77
pore volume fraction (%)	macropores	2.62−64.43	39.58	0−20.55	5.64	0−0	0
	mesopores	12.81−60.69	31.30	9.65−80.11	49.79	0−47.33	9.51
	micropores	9.06−64.01	29.12	11.51−90.35	44.57	52.67−100	90.49

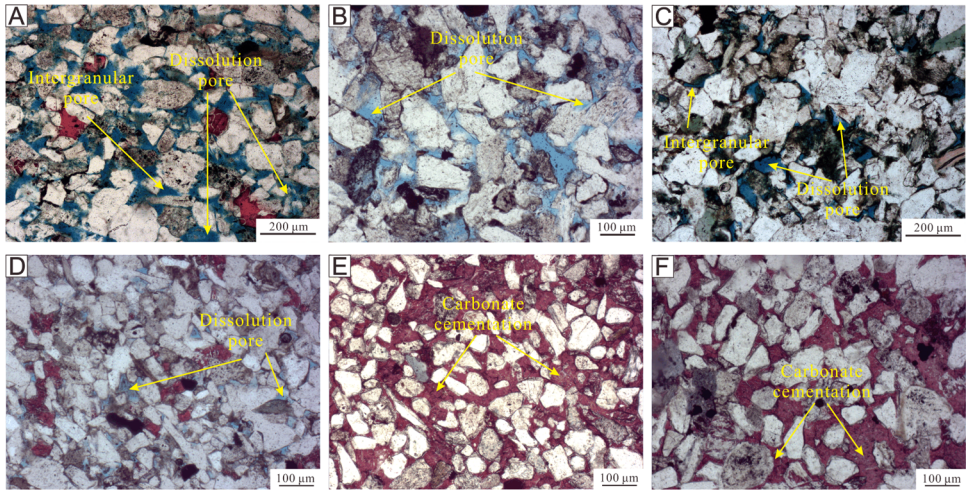

Figure 11. Microscopic characteristics for various types of pore structures. Type I: (A,B) Sandstones with abundant residual intergranular pores and dissolution pores, Well C371, 2691.95 m, and Well G890, 2597.7 m; Type II: (C,D) Sandstones with intergranular pores and dissolution pores, Well F119, 3292.55 m, and Well F153, 2818.4 m; Type III: (E,F) Extensive carbonate cementation, Well G351, 2464.79 m, and Well G890, 2621.1 m.

systems of the Type II pore structure are dominated by dissolution pores and intergranular pores (Figure 11C,D). Moreover, the micropores (<0.1 μm) and mesopores (0.1 < r < 1.0 μm) account for a great proportion in the Type II pore structure (Table 3). The Type III pore structure is characterized by the highest displacement pressure and the lowest FFI (Figure 10 and Table 3), which indicates a poor pore throat connectivity and fluid mobility. The sandstones dominated by the Type III pore structure are characterized by extensive carbonate cementation, with no visible pores under a petrographic microscope (Figure 11E,F). In addition, the Type II and Type III pore structures with a high proportion of small pores tend to have larger fractal dimensions compared with the Type I pore structures (Figure 10 and Table 3), indicating a more complex and heterogeneous pore structure.

5. DISCUSSION

5.1. Comparison of Fractal Dimensions from MICP and NMR Data. As can be seen from Section 4.2, the MICP tubular model is effective for fractal characterization. Nevertheless, for large pore systems, the calculated fractal dimension D_{T2} is not in conformance to the Euclidean dimension.[14,62] The MICP spherical model is only effective when $r_{min} \ll r$.[45,61] The model works well for the samples with large pore throats, but it is not suitable for fractal analysis of small pore systems (D_{S1} < 2.0). Moreover, the spherical model is more suitable for wetting phase intrusion measurements. It is effective for fractal analysis based on NMR data because water is a wetting phase commonly used in NMR experiments.

The comparative results also indicate that fractal dimensions determined from NMR and MICP data are different for given samples. The discrepancy may be caused by differences in theoretical principles and computation models of the two

https://doi.org/10.1021/acsomega.1c01015
ACS Omega 2021, 6, 11693−11710

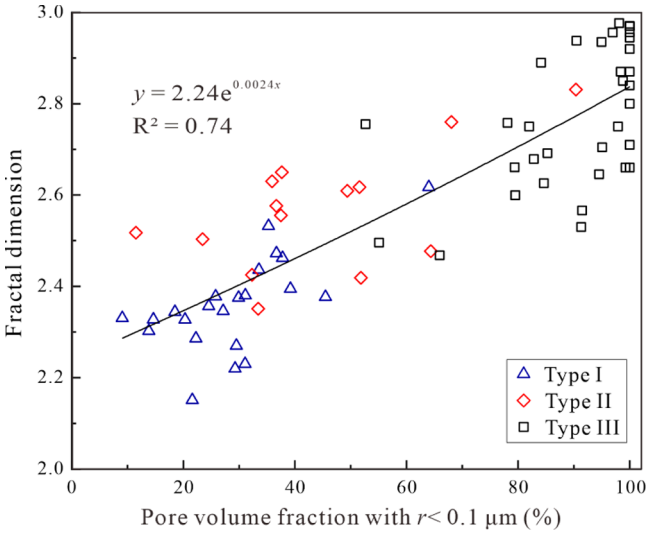

Figure 12. Relationships between fractal dimensions (D_T) and pore volume fraction of small pore throats (r < 0.1 μm).

different methods.[22,62] MICP fractal models are based on the pore throat sizes but cannot account for large pore throats. Due to the limitation of the maximum mercury injection pressure, the smallest part of the pore throat cannot be detected by the MICP measurements.[63] In contrast, NMR fractal dimensions can reflect the fractal behavior of entire pores (pore body sizes).[24] In addition, our investigations suggest that the sandstone samples with a high proportion of small pore throats often show larger fractal dimensions than those with abundant large pore throats (Figure 12). Therefore, the content of small pore throats may significantly control the pore throat heterogeneity.

5.2. Relationships between Pore Structure and Petrophysical Properties. *5.2.1. Analysis of Fractal Dimension and Reservoir Parameters.* Data from conventional core analysis of 70 samples reveal a positive correlation between porosity and permeability (R^2 = 0.71; Figure 13A). However, sandstone samples with similar porosities show wide variations in permeability (Figure 13A), suggesting that permeability of the low-permeability sandstones is not only determined by porosity but also influenced by their microscopic behaviors or other factors.

The relationships between petrophysical parameters, pore structure parameters, and fractal dimensions (e.g., porosity, permeability, RQI, r_{max}, r_{50}, sorting coefficient, T_{2gm}, T_{2peak}, and S_{wi}) were analyzed to illustrate the effect of fractal dimension on pore structure and reservoir quality evaluation. D_T exhibits a weak negative exponential correlation with helium porosity

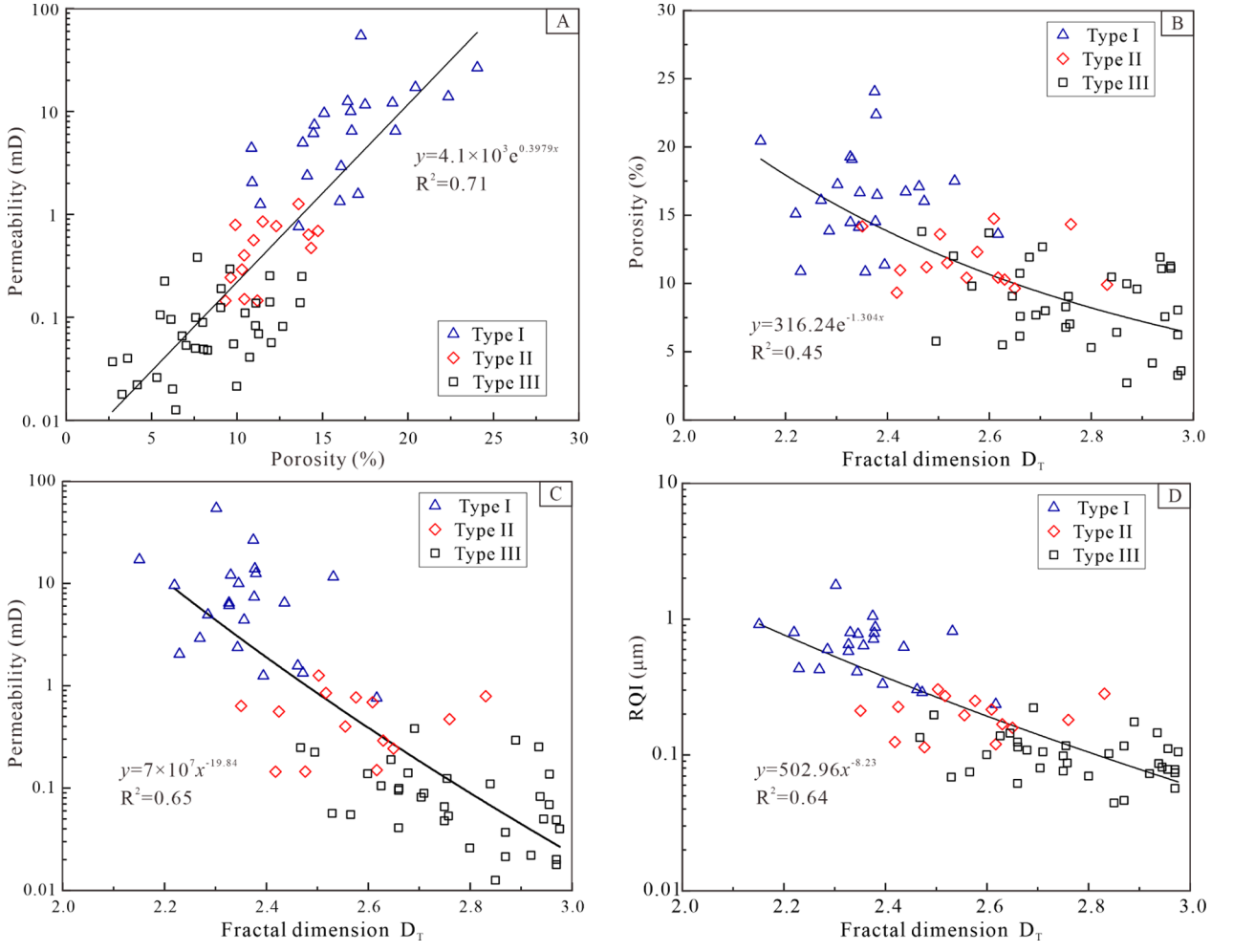

Figure 13. Relationships between fractal dimensions and petrophysical parameters. (A) Porosity vs permeability; (B) D_T vs helium porosity; (C) D_T vs air permeability; and (D) D_T vs RQI.

https://doi.org/10.1021/acsomega.1c01015
ACS Omega 2021, 6, 11693−11710

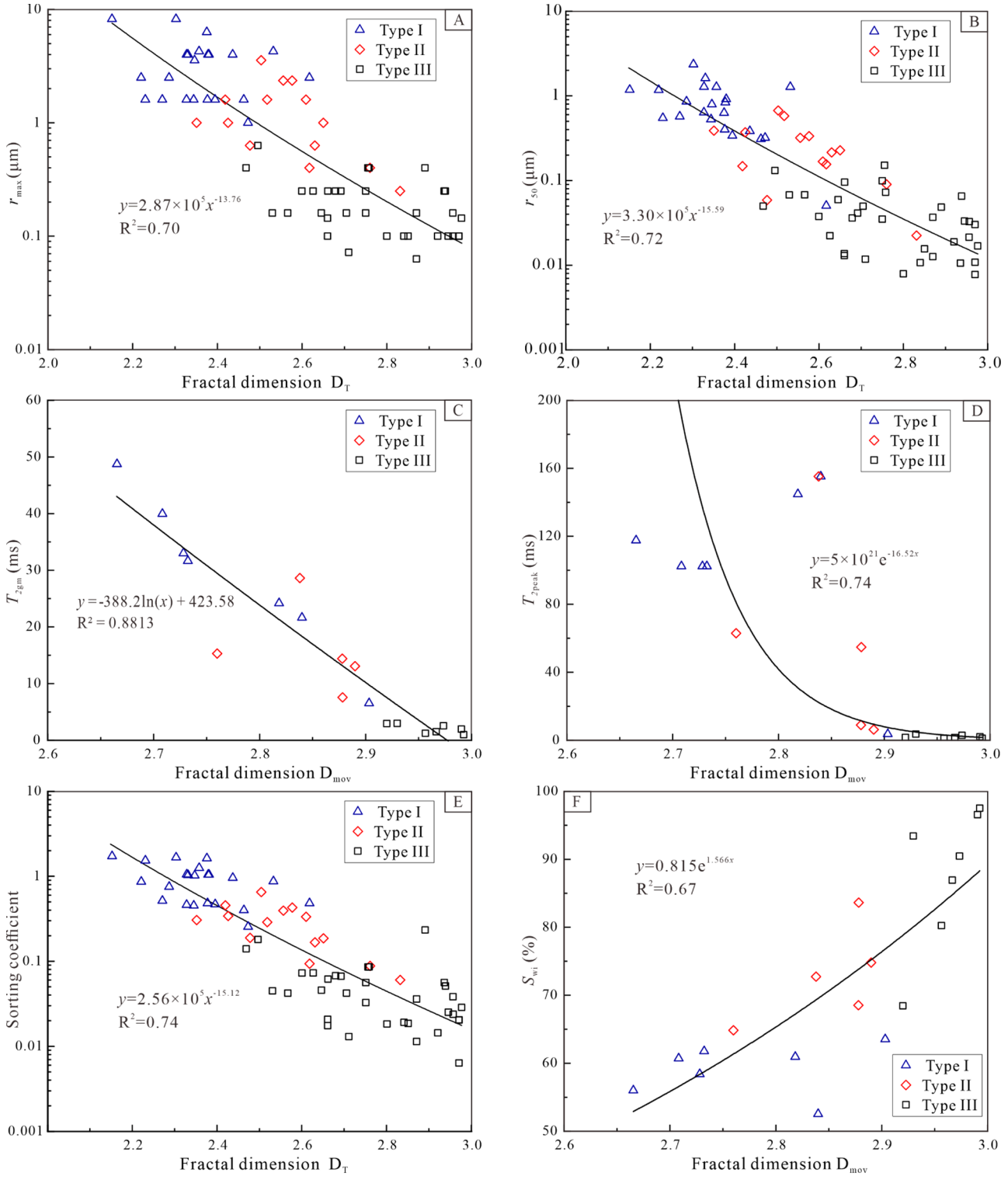

Figure 14. Cross-plots of fractal dimensions vs pore structure parameters. (A) D_T vs r_{max}; (B) D_T vs r_{50}; (C) D_{mov} vs T_{2gm}; (D) D_{mov} vs T_{2peak}; (E) D_T vs sorting coefficient; and (F) D_{mov} vs S_{wi}.

(R^2 = 0.45; Figure 13B), suggesting that higher D_T is often associated with lower porosity. In addition, regression analysis suggests that the D_T shows a relatively strong negative correlation with permeability (R^2 = 0.65; Figure 13C) and RQI (R^2 = 0.64; Figure 13D), implying an overall poor reservoir quality for reservoir sandstones with complex and heterogeneous pore structures.

As shown in Figure 14A,B, fractal dimension D_T is negatively correlated with r_{max} and r_{50} (R^2 > 0.70), suggesting that large pore throats and a concentrated pore throat size distribution would be helpful to reduce the complexity and heterogeneity of the pore structure.[14] This is also evident on Figure 14C,D, where both the T_{2gm} and T_{2peak} exhibit negative correlations with D_{mov}. Good correlations among sorting coefficients and fractal dimensions D_T are also observed (R^2 = 0.74; Figure

https://doi.org/10.1021/acsomega.1c01015
ACS Omega 2021, 6, 11693−11710

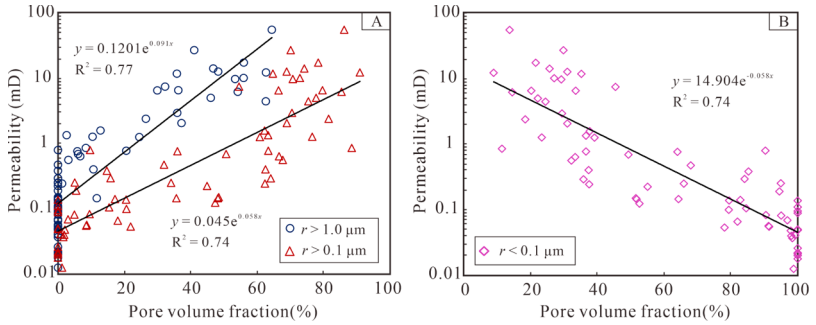

Figure 15. Relationships between permeability and pore volume fraction with different pore throat sizes. (A) permeability vs pore volume fraction for macropores and mesopores and (B) permeability vs pore volume for micropores.

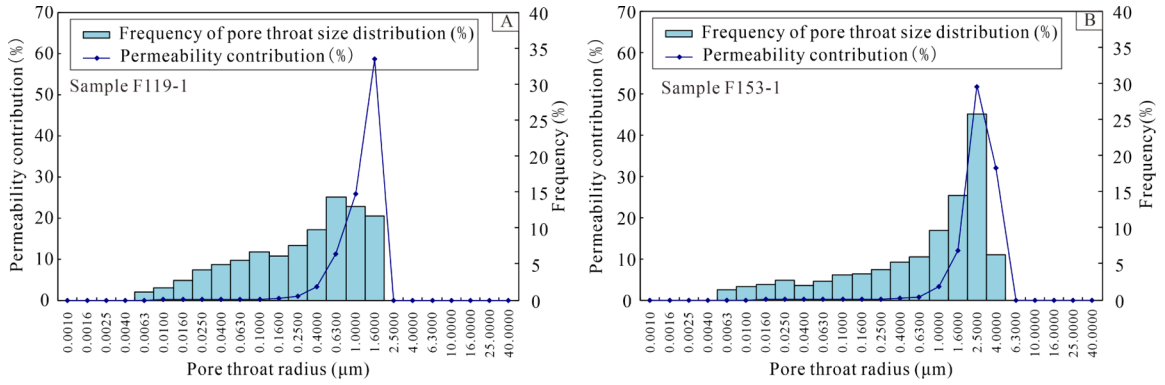

Figure 16. Pore throat size distribution and the corresponding permeability contribution for two typical samples from the E_{s4} sandstone reservoirs. (A) Sample F119-1, φ = 12.30%, k = 0.77 mD and (B) sample F153-1, φ = 10.85%, k = 4.40 mD.

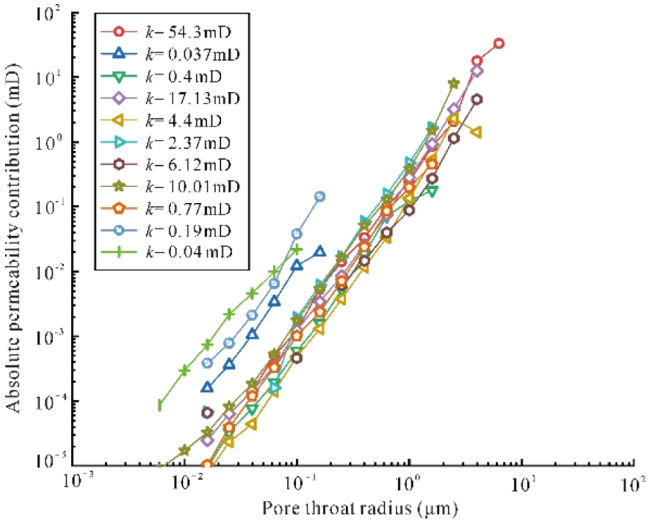

Figure 17. Cross-plot of pore throat radius and absolute permeability contribution obtained by MICP measurement, showing that the large pore systems contribute significantly to permeability.

14E), indicating the effectiveness of fractal dimensions in describing pore throat size distribution. D_{mov} shows positive correlations with S_{wi} with R^2 being 0.67 (Figure 14F). The larger the fractal dimension, the more complex the pore structure would be, leading to a poor pore throat connectivity and high irreducible water saturation.

The correlation analysis between the fractal dimensions (D_T and D_{mov}) and the reservoir parameters confirms a link between complex pore structure and petrophysical properties (Figures 13 and 14). Generally speaking, fractal dimensions can be used as important indicators for pore structure and reservoir heterogeneity evaluation. The complex process of pore structure characterization can therefore be simplified using fractal dimensions.[27,64] Furthermore, our studies have found that the fractal dimension D_S calculated using the MICP spherical model has no correlation with reservoir petrophysical properties and cannot reflect the complex and heterogeneous characteristics of the E_{s4} low-permeability sandstone reservoir.

5.2.2. Effect of the Pore Structure on Permeability. As shown in Figure 15A, there is a strong correlation between permeability and pore volume fraction with a pore throat radius larger than 0.1 and 1.0 μm. A negative correlation between permeability and pore volume fraction of micropores (r < 0.1 μm) is also observed in Figure 15B, indicating that micropores are generally disconnected or poorly connected in the pore network, consistent with the finding of Lai and Wang (2015).[14] The analytical results indicate that the large pore systems have significant contribution to permeability of the E_{s4} sandstone reservoirs (Figure 15A). Therefore, micropores have little contribution to reservoir permeability. Consequently, reservoir microscopic characteristics, especially the pore volume of large pores, can exert more significant effect on the permeability of the low-permeability sandstone reservoir.

As shown in Figures 16 and 17, the contribution of pore throats with different sizes to permeability has also been investigated. The result indicates that the large pore throats have great contribution to permeability, even though those pore throats usually account for a small proportion (Figure 16). The permeability contribution is significantly different in samples with different pore throat size distribution and permeability levels. The absolute permeability contribution increases with increasing pore throat radius (Figure 17), which

https://doi.org/10.1021/acsomega.1c01015
ACS Omega 2021, 6, 11693−11710

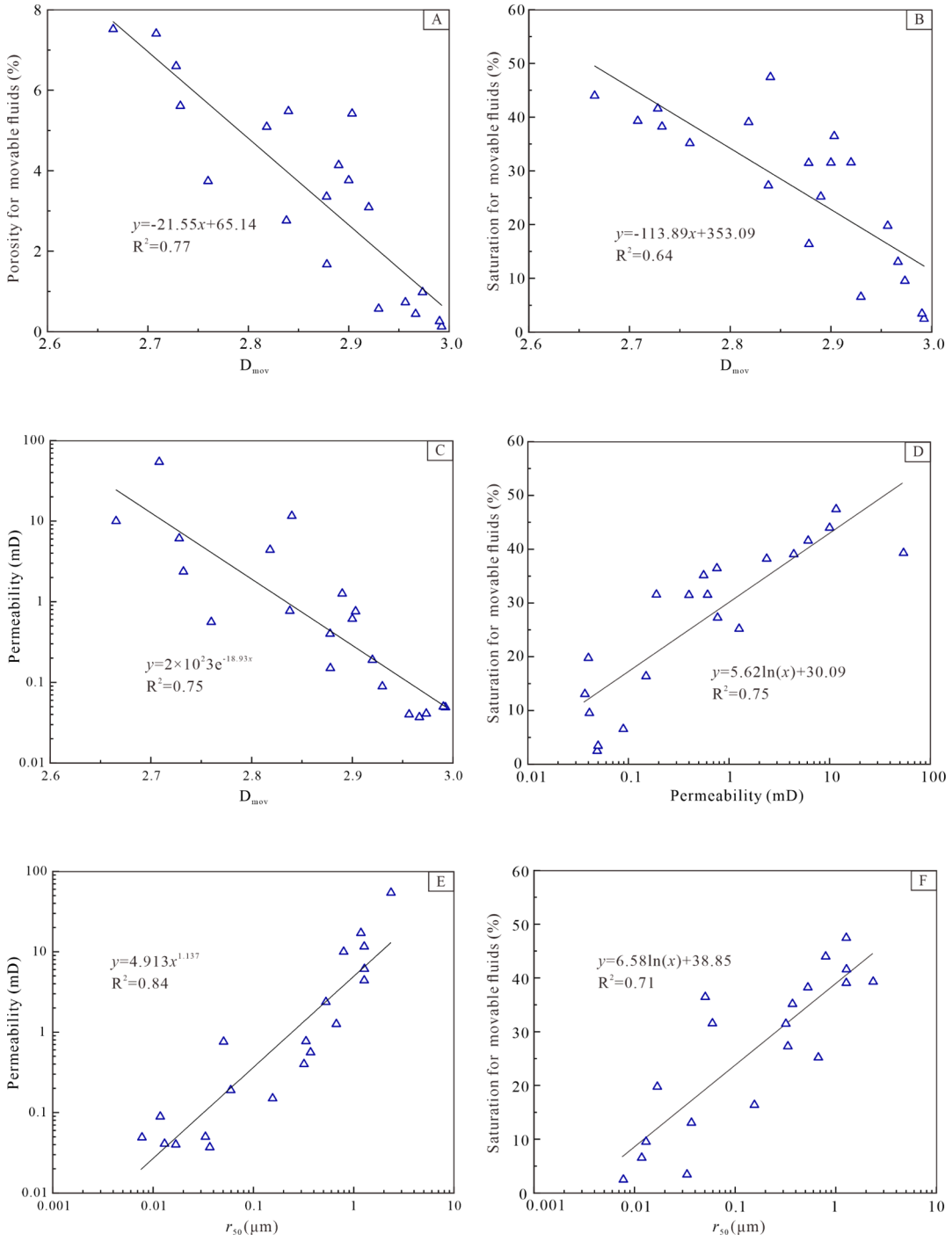

Figure 18. Relationship between pore structures and fluid mobility. (A) D_{mov} vs porosity for movable fluids; (B) D_{mov} vs saturation for movable fluids; (C) D_{mov} vs permeability; (D) permeability vs saturation for movable fluids; (E) r_{50} vs permeability; and (F) r_{50} vs saturation for movable fluids.

is the main reason for strong positive correlation between large pore systems and permeability (Figure 15A). As shown in Figure 17, the sandstone samples with higher permeability (>10 mD) always developed the pore throats with a radius greater than 2 μm. For samples with relatively low permeability (<0.1 mD), the r_{max} is commonly less than 1 μm.

5.2.3. Effect of the Pore Structure on Fluid Mobility. The fractal dimensions of movable fluid pores (D_{mov}) show positive correlations with porosity for a movable fluid (φ_m), saturation for movable fluids (S_{mov}), and permeability, with R^2 being 0.77, 0.64, and 0.75, respectively (Figure 18A–C). The larger the fractal dimension, the more complex the geometry of movable fluid pores, resulting in a poor pore throat connectivity and fluid mobility. In addition, permeability as the macroscopic performance of microscopic pore structures also show positive correlations with saturation for movable fluids (R^2 = 0.75; Figure 18D), indicating that with the improvement of petrophysical properties, the fluid mobility becomes better. Strong positive correlations were also observed between r_{50}, permeability, and saturation for a movable fluid (Figure

https://doi.org/10.1021/acsomega.1c01015
ACS Omega 2021, 6, 11693−11710

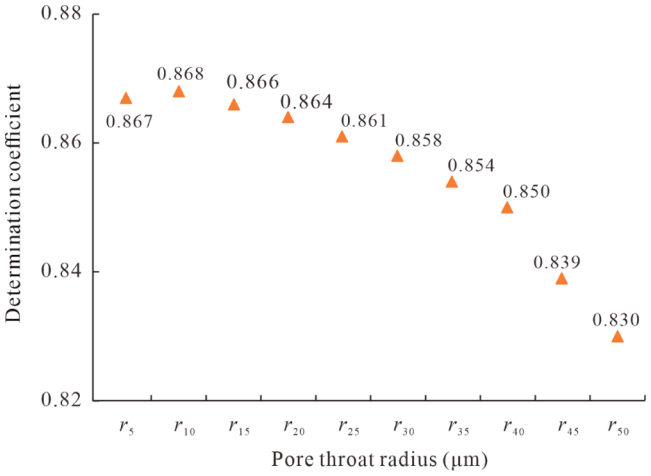

Figure 19. Determination coefficients corresponding to different pore throat radii (r_5−r_{50}). Note that r_{10} is strongly correlated with measured air permeability.

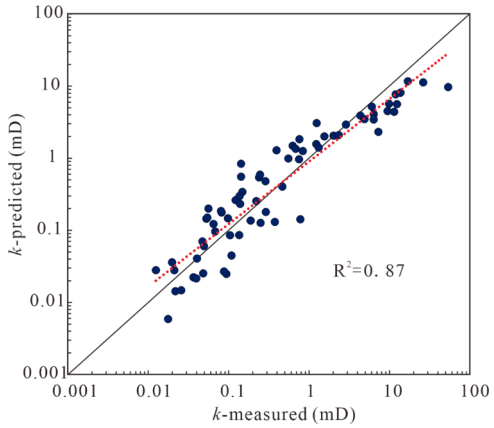

Figure 20. Cross-plot of k-measured vs k-predicted (R^2 = 0.87). The black solid line is the 1:1 line, while the red-dashed line marks the best fitting line between the k-measured and k-predicted.

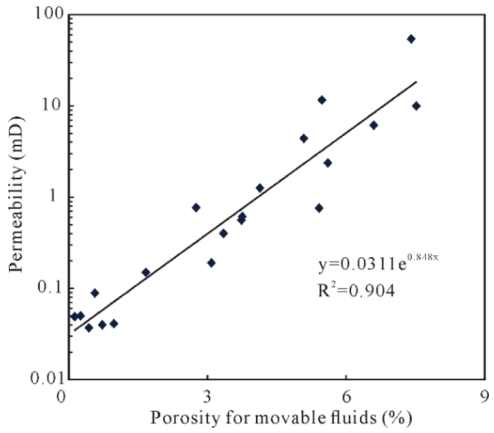

Figure 21. Relationship between porosity for movable fluids and measured permeability, showing an excellent fitting (R^2 = 0.90).

18E,F), confirming that the strong correlations between petrophysical properties and fluid mobility are greatly controlled by the large pore throats. The pore throat size distribution and pore connectivity have great influences on the permeability and fluid mobility in the pore network.

5.3. Permeability Estimation. *5.3.1. Permeability Estimation Based on the Modified Winland Model.* Due to the intrinsic strong correlation between permeability and pore throat size distribution, the permeability estimation models based on the pore throat radius usually show a better prediction effect.[65,66] The Winland model described the relationship between permeability, pore throat radius, and porosity.[30] The model indicates that permeability of high-permeability reservoirs is mainly controlled by the r_{35} pore throat value. Several authors further extended the concept and found that the optimal pore throat radius for permeability estimation varies for different types of reservoirs.[37,67,68] Through the multiple regression analysis of permeability, porosity, and pore throat radius (r_5−r_{50}), we demonstrated that the r_{10} is the best value for permeability estimation of the E_{s4} low-permeability sandstone reservoirs (Figure 19). The r_{10} parameter was selected for permeability estimation, which was dominated by the pore throat size mainly concentrated between 0.1 and 5.0 μm, corresponding to the large pore systems. The empirical equation (eq 16) is shown as follows

$$\log k = -1.306 + 1.238 \times \log \varphi + 0.982 \times \log r_{10} \quad (16)$$

where k is the measured permeability (mD); φ is the helium porosity (%); and r_{10} is the pore throat radius corresponding to 10% of the cumulative mercury saturation (μm).

As shown in Figure 20, the predicted permeability (k-predicted) is in good correlation with the measured permeability (k-measured) (R^2 = 0.87), indicating the effectiveness of the permeability estimation model. Moreover, the pore throat radius can also be predicted by permeability and porosity based on the established empirical equation.

5.3.2. Permeability Estimation Based on the Porosity Model Derived from Movable Fluids. As shown in Section 5.2.2, the disconnected or poorly connected pores in sandstone have little contribution to permeability. Hence, the porosity for movable fluids (φ_m) is recommended for permeability estimation rather than the total porosity,[16,23] and φ_m can be calculated using eq 17. Regression analysis shows that the φ_m exhibits a strong exponential correlation with permeability (R^2 = 0.90; Figure 21). The permeability estimation model based on φ_m is shown in eq 18.

$$\varphi_m = \varphi_N \times \mathrm{FFI}/(\mathrm{BVI} + \mathrm{FFI}) \quad (17)$$

$$k = 0.0311 \times e^{0.848 \times \varphi_m} \quad (18)$$

where φ_N is the NMR porosity and FFI and BVI are the free fluid index and bulk volume of the immovable fluid, respectively.

The predicted permeability of the sandstone samples is calculated using eq 18. As shown in Figure 22B, the predicted values are in good agreement with measured values with little difference (Figure 22B). We also shed light on the permeability estimation using the classic (Coates and SDR) models (Figure 22A). The porosity model derived from movable fluids provides a better estimation effect compared with the classic models (Table 4; Figure 22), implying the effectiveness and applicability of the new model for permeability estimation.

6. CONCLUSIONS

The microscopic pore structure of the Eocene low-permeability sandstones was investigated based on NMR and MICP data in combination with fractal theory and self-organizing map (SOM) neural network algorithm. Two permeability

https://doi.org/10.1021/acsomega.1c01015
ACS Omega 2021, 6, 11693−11710

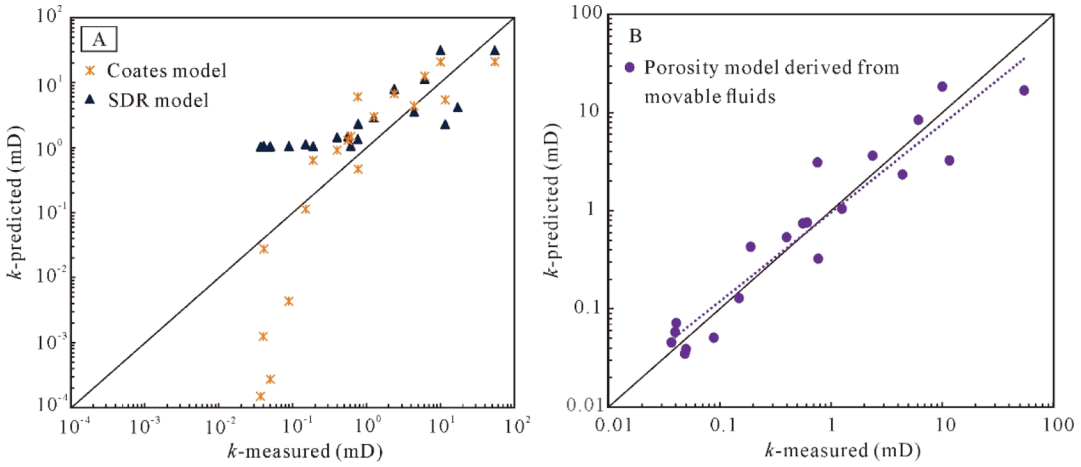

Figure 22. Cross-plots of *k*-measured vs *k*-predicted. (A) Coates and SDR models and (B) porosity model derived from movable fluids.

Table 4. Fitting Equations and Determination Coefficients for Three Different Permeability Estimation Models Using NMR Data

permeability estimation model	fitting equation	determination coefficient
Coates model	$k = (\varphi_N/0.0675)^4 \times (FFI/BVI)^2$	0.75
SDR model	$k = 14.901 \times \varphi_N^4 T_{2g}^2$	0.55
porosity model derived from movable fluids	$k = 0.0311 \times e^{0.843\varphi_m}$	0.90

estimation models were established based on the pore structure information obtained from MICP and NMR measurements. Some key findings are as follows:

(1) SOM, an unsupervised neural network clustering algorithm, was adopted to investigate the pore structures. Three types of pore structures had been identified using an established SOM clustering model. Type I and II pore structures are dominated by large pore throats with good pore throat connectivity and contribute significantly to the permeability. Type III pore structures are characterized by abundant small pore throats and a poor pore throat connectivity and are unfavorable for the fluid flow.

(2) The MICP tubular model is effective for fractal characterization, and the fractal dimensions calculated using the tubular model exhibit strong correlations with petrophysical parameters and pore structure parameters. The fractal dimensions derived from the MICP spherical model are not recommended for pore structure and reservoir quality evaluation. The spherical model is more suitable for fractal analysis based on NMR data because water is a wetting phase commonly used in NMR experiments.

(3) The fractal dimensions of the reservoirs investigated, D_T and D_{NMR}, are in the range of 2.15−2.98 and 2.14−2.60, respectively. The discrepancy may be caused by the difference in theoretical principles and calculation models of the two different types of measurements. Samples with high proportions of small pore throats often show larger fractal dimensions, indicating that the pore volume of the small pore throats significantly controls the pore throat connectivity and heterogeneity of the sandstone reservoirs.

(4) Regression analysis indicates that r_{10} is the best parameter for permeability estimation, which has a concentrated distribution of 0.1−5.0 μm, indicating that the large pore systems have a significant control on the fluid flow in the Eocene low-permeability sandstones. Another permeability estimation model based on φ_m has also been established, which provides a better prediction effect than the classic models. These findings are vital for investigating the fluid flow mechanism and predicting the reservoir quality of the Eocene sandstone reservoirs.

AUTHOR INFORMATION

Corresponding Author

Keyu Liu − *School of Geosciences and Key Laboratory of Deep Oil and Gas, China University of Petroleum (East China), Qingdao 266580, China; CSIRO Energy, Kensington, Western Australia 6151, Australia;* orcid.org/0000-0002-8741-9802; Email: liukeyu@upc.edu.cn

Author

Yan Lu − *School of Geosciences and Key Laboratory of Deep Oil and Gas, China University of Petroleum (East China), Qingdao 266580, China;* orcid.org/0000-0003-0043-6237

Complete contact information is available at: https://pubs.acs.org/10.1021/acsomega.1c01015

Notes

The authors declare no competing financial interest.

ACKNOWLEDGMENTS

This work was financially supported by the program of the National Science and Technology Major Project of China (no. 2017ZX05009001), the Strategic Priority Research Program of the Chinese Academy of Sciences (no. XDA14010401), and the National Natural Science Foundation of China (grant no. 41821002).

REFERENCES

(1) Zahid, M. A.; Chunmei, D.; Lin, C.; Gluyas, J.; Jones, S.; Zhang, X.; Munawar, M. J.; Ma, C. Sequence stratigraphy, sedimentary facies

https://doi.org/10.1021/acsomega.1c01015
ACS Omega 2021, 6, 11693−11710

and reservoir quality of Es4s, southern slope of Dongying Depression, Bohai Bay Basin, East China. *Mar. Petrol. Geol.* **2016**, *77*, 448−470.
(2) Zhang, S.; Fang, Z. Permeability damage micro-mechanisms and stimulation of low-permeability sandstone reservoirs: A case study from Jiyang Depression, Bohai Bay Basin. China. *Pet. Explor. Dev.* **2020**, *47*, 374−382.
(3) Qing, F.; Yan, J.; Wang, J.; Hu, Q.; Wang, M.; Geng, B.; Chao, J. Pore structure and fluid saturation of near-oil source low-permeability turbidite sandstone of the Dongying Sag in the Bohai Bay Basin, East China. *J. Pet. Sci. Eng.* **2021**, *196*, 108106.
(4) Chen, Q.; Song, Y.-Q. What is the shape of pores in natural rocks? *J. Chem. Phys.* **2002**, *116*, 8247−8250.
(5) Boer, R. Reflections on the development of the theory of porous media. *Appl. Mech. Rev.* **2003**, *56*, R27−R42.
(6) Zhang, Z.; Qin, Y.; Yi, T.; You, Z.; Yang, Z. Pore structure characteristics of coal and their geological controlling factors in Eastern Yunnan and Western Guizhou, China. *ACS Omega* **2020**, *5*, 19565−19578.
(7) Mandelbrot, B. B. *Fractals: Form, Chance, and Dimension: Freeman*; Cleave Cambridge University Press: San Francisco, 1977; pp 1−361.
(8) Poulton, M. M.; Mojtabai, N.; Farmer, I. W. Scale invariant behaviour of massive and fragmented rock. *Int. J. Rock Mech. Min.* **1990**, *27*, 219−221.
(9) Hansen, J. P.; Skjeltorp, A. T. Fractal pore space and rock permeability implications. *Phys. Rev. B: Condens. Matter Mater. Phys.* **1988**, *38*, 2635−2638.
(10) Guo, Y.; Zhou, L.; Guo, F.; Chen, X.; Wu, J.; Zhang, Y. Pore structure and fractal characteristic analysis of gasification-coke prepared at different high-temperature residence times. *ACS Omega* **2020**, *5*, 22226−22237.
(11) Sakhaee-Pour, A.; Li, W. Fractal dimensions of shale. *J. Nat. Gas Sci. Eng.* **2016**, *30*, 578−582.
(12) Daigle, H.; Johnson, A.; Thomas, B. Determining fractal dimension from nuclear magnetic resonance data in rocks with internal magnetic field gradients. *Geophysics* **2014**, *79*, D425−D431.
(13) Liu, X.; Nie, B. Fractal characteristics of coal samples utilizing image analysis and gas adsorption. *Fuel* **2016**, *182*, 314−322.
(14) Lai, J.; Wang, G. Fractal analysis of tight gas sandstones using high-pressure mercury intrusion techniques. *J. Nat. Gas Sci. Eng.* **2015**, *24*, 185−196.
(15) Stallmach, F.; Vogt, C.; Kärger, J.; Helbig, K.; Jacobs, F. Fractal geometry of surface areas of sand grains probed by pulsed eld gradient NMR. *Phys. Rev. Lett.* **2002**, *88*, 105505.
(16) Zheng, S.; Yao, Y.; Liu, D.; Cai, Y.; Liu, Y. Characterizations of full-scale pore size distribution, porosity and permeability of coals: A novel methodology by nuclear magnetic resonance and fractal analysis theory. *Int. J. Coal Geol.* **2018**, *196*, 148−158.
(17) Qiu, S.; Yang, M.; Xu, P.; Rao, B. A new fractal model for porous media based on low-field nuclear magnetic resonance. *J. Hydrol.* **2020**, *586*, 124890.
(18) Schmitt Rahner, M.; Halisch, M.; Peres Fernandes, C.; Weller, A.; Sampaio Santiago dos Santos, V. Fractal dimensions of pore spaces in unconventional reservoir rocks using X-ray nano- and micro-computed tomography. *J. Nat. Gas Sci. Eng.* **2018**, *55*, 298−311.
(19) Xia, Y.; Cai, J.; Perfect, E.; Wei, W.; Zhang, Q.; Meng, Q. Fractal dimension, lacunarity and succolarity analyses on CT images of reservoir rocks for permeability prediction. *J. Hydrol.* **2019**, *579*, 124198.
(20) Schmitt, M.; Fernandes, C. P.; Da Cunha Neto, J. A. B.; Wolf, F. G.; Dos Santos, V. S. S. Characterization of pore systems in seal rocks using nitrogen gas adsorption combined with mercury injection capillary pressure techniques. *Mar. Pet. Geol.* **2013**, *39*, 138−149.
(21) Li, T.; Wu, J.-j.; Cai, Y.-g.; Wang, X.; Huang, H. Particle size effect and temperature effect on the pore structure of low-rank coal. *ACS Omega* **2021**, *6*, 5865.
(22) Li, W.; Zhao, H.; Li, S.; Sun, W.; Wang, L.; Li, B. A fractal model of effective stress of porous media and the analysis of influence factors. *Results Phys.* **2018**, *8*, 920−925.
(23) Li, Z.; Liu, D.; Cai, Y.; Wang, Y.; Si, G. Evaluation of coal petrophysics incorporating fractal characteristics by mercury intrusion porosimetry and low-field NMR. *Fuel* **2020**, *263*, 116802.
(24) Sigal, R. F. Pore-size distributions for organic-shale-reservoir rocks from nuclear-magnetic-resonance spectra combined with adsorption measurements. *SPE J.* **2015**, *20*, 824−830.
(25) Peng, C.; Zou, C.; Yang, Y.; Zhang, G.; Wang, W. Fractal analysis of high rank coal from southeast Qinshui basin by using gas adsorption and mercury porosimetry. *J. Petrol. Sci. Eng.* **2017**, *156*, 235−249.
(26) Zhao, Y.; Zhu, G.; Dong, Y.; Danesh, N. N.; Chen, Z.; Zhang, T. Comparison of low-field NMR and microfocus X-ray computed tomography in fractal characterization of pores in artificial cores. *Fuel* **2017**, *210*, 217−226.
(27) Guo, X.; Huang, Z.; Zhao, L.; Han, W.; Ding, C.; Sun, X.; Yan, R.; Zhang, T.; Yang, X.; Wang, R. Pore structure and multi-fractal analysis of tight sandstone using MIP, NMR and NMRC methods: A case study from the Kuqa depression, China. *J. Pet. Sci. Eng.* **2019**, *178*, 544−558.
(28) Yan, J.; Fan, J.; Wang, M.; Li, Z.; Hu, Q.; Chao, J. Rock fabric and pore structure of the Shahejie sandy conglomerates from the Dongying Depression in the Bohai Bay Basin, East China. *Mar. Petrol. Geol.* **2018**, *97*, 624−638.
(29) Kolodzie, S. Analysis of pore throat size and use of the Waxman-Smits equation to determine OOIP in Spindle Field, Colorado. *SPE Annual Technical Conference and Exhibition*. September 21−24: Dallas, Texas, 1980. SPE-9382-MS.
(30) Coates, G. R.; Peveraro, R. C. A.; Hardwick, A.; Roberts, D. The magnetic resonance imaging log characterized by comparison with petrophysical properties and laboratory core data. *SPE Annual Technical Conference and Exhibition*. October 6−9: Dallas, Texas, 1991. SPE-22723-MS.
(31) Glover, P. W.; Zadjali, I. I.; Frew, K. A. Permeability prediction from MICP and NMR data using an electrokinetic approach. *Geophysics* **2006**, *71*, F49−F60.
(32) Schmitt, M.; Fernandes, C. P.; Wolf, F. G.; Bellini da Cunha Neto, J. A.; Rahner, C. P.; Santiago dos Santos, V. S. Characterization of Brazilian tight gas sandstones relating permeability and angstrom-to micron-scale pore structures. *J. Nat. Gas Sci. Eng.* **2015**, *27*, 785−807.
(33) Kozeny, J. Über kapillare Leitung des Wassers im Boden. *Sitzungsber. Akad. Wiss. Wien* **1927**, *136*, 271−306.
(34) Carman, P. C. Fluid flow through granular beds. *Trans. Inst. Chem. Eng.* **1937**, *15*, 150−166.
(35) Pape, H.; Clauser, C.; Iffland, J. Permeability prediction based on fractal pore-space geometry. *Geophysics* **1999**, *64*, 1447−1460.
(36) Pittman, E. D. Relationship of porosity and permeability to various parameters derived from mercury injection-capillary pressure curves for sandstone. *AAPG Bull.* **1992**, *76*, 191−198.
(37) Rezaee, R.; Saeedi, A.; Clennell, B. Tight gas sands permeability estimation from mercury injection capillary pressure and nuclear magnetic resonance data. *J. Pet. Sci. Eng.* **2012**, *88*−*89*, 92−99.
(38) Loucks, R. G.; Dutton, S. P. Insights into deep, onshore Gulf of Mexico Wilcox sandstone pore networks and reservoir quality through the integration of petrographic, porosity and permeability, and mercury injection capillary pressure analyses. *AAPG Bull.* **2019**, *103*, 745−765.
(39) Lu, Y.; Liu, K.; Xu, S.; Wang, Y.; Zhang, Q. Identifying flow units by FA-assisted SSOM-An example from the Eocene basin-floor-fan turbidite reservoirs in the Daluhu Oilfield, Dongying Depression, Bohai Bay Basin, China. *J. Pet. Sci. Eng.* **2020**, *186*, 106695.
(40) Lampe, C.; Song, G.; Cong, L.; Mu, X. Fault control on hydrocarbon migration and accumulation in the Tertiary Dongying depression, Bohai Basin, China. *AAPG Bull.* **2012**, *96*, 983−1000.
(41) Avnir, D.; Farin, D.; Pfeifer, P. Molecular fractal surfaces. *Nature* **1984**, *308*, 261−263.
(42) Davis, H. T. On the fractal character of the porosity of natural sandstone. *Europhys. Lett.* **1989**, *8*, 629−632.

https://doi.org/10.1021/acsomega.1c01015
ACS Omega 2021, 6, 11693−11710

(43) Daigle, H.; Johnson, A. Combining mercury intrusion and nuclear magnetic resonance measurements using percolation theory. *Transp. Porous Media* **2016**, *111*, 669−679.
(44) Mandelbrot, B. B.; Passoja, D. E.; Paullay, A. J. Fractal character of fracture surfaces of metals. *Nature* **1984**, *308*, 721−722.
(45) Zhang, Z.; Weller, A. Fractal dimension of pore-space geometry of an Eocene sandstone formation. *Geophysics* **2014**, *79*, D377−D387.
(46) Wang, F.; Yang, K.; You, J.; Lei, X. Analysis of pore size distribution and fractal dimension in tight sandstone with mercury intrusion porosimetry. *Results Phys.* **2019**, *13*, 102283.
(47) Lai, J.; Wang, G.; Fan, Z.; Zhou, Z.; Chen, J.; Wang, S. Fractal analysis of tight shaly sandstones using nuclear magnetic resonance measurements. *AAPG Bull.* **2018**, *102*, 175−193.
(48) Kohonen, T. Self-organized formation of topologically correct feature maps. *Biol. Cybern.* **1982**, *43*, 59−69.
(49) Pandit, Y. P.; Badhe, Y. P.; Sharma, B. K.; Tambe, S. S.; Kulkarni, B. D. Classification of Indian power coals using k-means clustering and Self Organizing Map neural network. *Fuel* **2011**, *90*, 339−347.
(50) Saraswat, P.; Sen, M. K. Artificial immune-based self-organizing maps for seismic-facies analysis. *Geophysics* **2012**, *77*, O45−O53.
(51) Bauer, K.; Kulenkampff, J.; Henninges, J.; Spangenberg, E. Lithological control on gas hydrate saturation as revealed by signal classification of NMR logging data. *J. Geophys. Res.: Solid Earth* **2015**, *120*, 6001−6017.
(52) Chang, H.-C.; Kopaska-Merkel, D. C.; Chen, H.-C. Identification of lithofacies using Kohonen self-organizing maps. *Comput. Geosci.* **2002**, *28*, 223−229.
(53) Bierlein, F. P.; Fraser, S. J.; Brown, W. M.; Lees, T. Advanced methodologies for the analysis of databases of mineral deposits and major faults. *Aust. J. Earth Sci.* **2008**, *55*, 79−99.
(54) Liu, X.; Mutailipu, M.; Zhao, J.; Liu, Y. Comparative Analysis of Four Neural Network Models on the Estimation of CO2-Brine Interfacial Tension. *ACS Omega* **2021**, *6*, 4282−4288.
(55) Lai, J.; Wang, G.; Cao, J.; Xiao, C.; Wang, S.; Pang, X.; Dai, Q.; He, Z.; Fan, X.; Yang, L.; Qin, Z. Investigation of pore structure and petrophysical property in tight sandstones. *Mar. Petrol. Geol.* **2018**, *91*, 179−189.
(56) Pape, H.; Clauser, C. Improved Interpretation of Nuclear Magnetic Resonance T_1 and T_2 Distributions for Permeability Prediction: Simulation of Diffusion Coupling for a Fractal Cluster of Pores. *Pure Appl. Geophys.* **2009**, *166*, 949−968.
(57) Rosenbrand, E.; Fabricius, I. L.; Fisher, Q.; Grattoni, C. Permeability in Rotliegend gas sandstones to gas and brine as predicted from NMR, mercury injection and image analysis. *Mar. Pet. Geol.* **2015**, *64*, 189−202.
(58) Saidian, M.; Prasad, M. Effect of mineralogy on nuclear magnetic resonance surface relaxivity: A case study of Middle Bakken and Three Forks formations. *Fuel* **2015**, *161*, 197−206.
(59) Pfeifer, P.; Avnir, D. Chemistry in noninteger dimensions between 2 and 3. *J. Chem. Phys.* **1983**, *79*, 3558−3565.
(60) Lai, J.; Wang, G.; Wang, Z.; Chen, J.; Pang, X.; Wang, S.; Zhou, Z.; He, Z.; Qin, Z.; Fan, X. A review on pore structure characterization in tight sandstones. *Earth Sci. Rev.* **2018**, *177*, 436−457.
(61) Ouyang, Z.; Liu, D.; Cai, Y.; Yao, Y. Fractal analysis on heterogeneity of pore-fractures in middle-high rank coals with NMR. *Energy Fuels* **2016**, *30*, 5449−5458.
(62) Zhu, F.; Hu, W.; Cao, J.; Sun, F.; Liu, Y.; Sun, Z. Micro/nanoscale pore structure and fractal characteristics of tight gas sandstone: a case study from the Yuanba area, northeast Sichuan basin, China. *Mar. Pet. Geol.* **2018**, *98*, 116−132.
(63) Mahamud, M. M.; Novo, M. F. The use of fractal analysis in the textural characterization of coals. *Fuel* **2008**, *87*, 222−231.
(64) Giri, A.; Tarafdar, S.; Gouze, P.; Dutta, T. Fractal pore structure of sedimentary rocks: simulation in 2-d using a relaxed bidisperse ballistic deposition model. *J. Appl. Geophys.* **2012**, *87*, 40−45.
(65) Swanson, B. F. A simple correlation between permeabilities and mercury capillary pressures. *J. Pet. Technol.* **1981**, *33*, 2498−2504.
(66) Katz, A. J.; Thompson, A. H. Quantitative prediction of permeability in porous rock. *Phys. Rev. B: Condens. Matter Mater. Phys.* **1986**, *34*, 8179−8181.
(67) Martin, A. J.; Solomon, S. T.; Hartmann, D. J. Characterization of Petrophysical Flow Units in Carbonate Reservoirs. *AAPG Bull.* **1997**, *81*, 734−759.
(68) Rezaee, M. R.; Jafari, A.; Kazemzadeh, E. Relationships between permeability, porosity and pore throat size in carbonate rocks using regression analysis and neural networks. *J. Geophys. Eng.* **2006**, *3*, 370−376.

https://doi.org/10.1021/acsomega.1c01015
ACS Omega 2021, 6, 11693−11710